Department of Precision and Microsystems Engineering

A Compact Ultra-Linear Compliant Torsion Reinforced Sarrus Mechanism

Joran van Velden

Report no	: 2024.022
Coach	: E. de Groot, VDL ETG T&D
Professor	: Prof. dr. ir. J.L. Herder
Specialisation	: Mechatronic System Design
Type of report	: Master Thesis
Date	: May 8, 2024

A Compact Ultra-Linear Compliant Torsion Reinforced Sarrus Mechanism

by

J.L. van Velden

to obtain the degree of Master of Science
at the Delft University of Technology,
to be defended publicly on Friday May 17, 2024 at 15:00.

Student number:	4722809	
Project duration:	October 1, 2022 – May 17, 2024	
Thesis committee:	Prof. dr. ir. J.L. Herder,	TU Delft, chair and supervisor
	E. de Groot,	VDL ETG T&D , daily supervisor
	Dr. S. Kumar,	TU Delft
	Ir. T.A. Baaij,	TU Delft

TU Delft

Preface

In completing this master thesis, I have had the privilege of delving into a topic that has both challenged and inspired me. This work is the result of a great collaboration between TU Delft, VDL ETG T&D, and myself. The level of autonomy and confidence within the company and university lead to a result where I am proud of: this master thesis and a pending patent.

I would like to express my gratitude to Edwin de Groot, my daily supervisor, and Just Herder, my professor and supervisor, whose guidance and support were invaluable throughout this project. Their expertise, encouragement, and constructive feedback have played a pivotal role in shaping this thesis.

I owe a debt of gratitude to my collegues at VDL ETG T&D whose insights and assistance were instrumental in various stages of this project. Their contributions have enriched my understanding and have undoubtedly improved the quality of this work.

I must also acknowledge the support of my family, girlfriend, and friends, whose encouragement, curiosity, and positivity have been a constant source of strength.

This thesis is a testament to the collaborative efforts of many individuals. Thank you all.

J.L. van Velden
Nieuwegein, May 2024

Contents

1

Literature Review

An Overview of Compliant one Translational Degree of Freedom Nanopositioners and their Parasitic Motions

Submitted on 30/01/2024
authored by
Joran van Velden
supervised by
Just Herder

Index Terms—**Compliant, 1-DoF, Precision, nanopositioner, Parasitic Motion**

Abstract—**This paper presents an extensive review of compliant one-degree-of-freedom nanopositioners, focusing on various mechanisms and flexures employed in these systems. The study explores strategies to mitigate parasitic motion and compares nanopositioners based on key performance metrics. The results highlight specific mechanisms and their performance, considering translational and rotational parasitic motions. Noteworthy findings include the scarcity of literature on compliant nanopositioners, the benefits of certain strategies in minimizing parasitic motions, and the promising potential of spatial mechanisms for nanopositioning, despite increased complexity. The need for well-constrained, compact designs that leverage parasitic motion strategies to achieve nanometer-level accuracy and extensive measurement in all directions is emphasized.**

I. Introduction

Ultra-precision mechanisms with up to six degrees of freedom (DoF) motion are the foundation for applications like semiconductor fabrication [1][2], scanning systems [3][4], medical imaging [5], and fabrication of nano-devices [6][7]. These industries demand devices that allow for precision motion guidance with a resolution and accuracy in the order of micrometers or even nanometers. For example, in the semiconductor industry the trend is to make the microchips smaller and faster, with even a resolution of 20nm leading to a need for more accurate precision guidance [8]. Parasitic motion and cross-axis couplings reduce the precision, efficiency and increases the control complexity. Therefore, there is a high demand for straight motion technology.

There are many existing technologies for straight motion. The guideway or bearing separates the moving part from the fixed part which makes it the most critical part. Bearings can be divided into two classes, contact and non contact bearing systems. Sliding bearings and ball bearings are examples of contact bearing systems. Compliant mechanisms, hydro/aerostatic, hydro/aerodynamic, and magnetic bearings are examples of non contact bearing systems. Contact bearings will introduce wear and friction which implies hysteresis and less reliability which makes them unsuitable for repeatable ultra-precision straight motion. Hydrostatic and aerostatic bearings are well-known for ultra-precision manipulation. Their characteristics are beneficial for precise motion over a long stroke, as there is no mechanical contact and they can obtain high accuracy due to the surface averaging effect [9]. However, they introduce complexities to the system and usage of liquids in clean environments is unwanted. An external compressor is needed for the gas or liquid supply, and the gas supply will introduce pressure ripple that give a position uncertainty of typically 50nm [10]. Furthermore, vertical applications of aerostatic bearings face difficulties with straightness. The gravity load working on the system induces sagging [11]. To overcome

most of the above described problems, compliant mechanisms can be used.

Compliant mechanisms (CM) use elastic deformation of flexible components to allow a desired motion due to a force or input motion. There are multiple advantages of compliant mechanisms which are preferable for precise positioning. Advantages are that due to elastic deformation these mechanisms have no friction, backlash, and are linearly predictable for small motions[12]. Furthermore, CM benefit from the fact that there are usually no overlapping pieces which allow a single piece production [13]. This has a potential for significantly lower costs, due to less assembly and manufacturing time, resulting in that they are well-known in positioning stages for small ranges. However, CM are more challenging to design due to their inherent coupling between kinetics and kinematics[14].

There are many known straight-line mechanisms, that could be transformed to compliant mechanisms. Examples of these are the Roberts [15], Watt's [16], and Sarrus Linkages [17] and the Scott-Russel [18][19], Roberts-Chebyshev [20], Peaucellier [21], and 13-Hinge mechanisms [17]. Furthermore, parallelograms consisting of leaf springs in a multiple of two in parallel attached to a body are widely used. In theory, these mechanisms approximately or exactly describe a straight line. However, in practice certain deviations along a straight line are observed.

To reduce possible deviations from a straight line, certain strategies can be used. The strategies include symmetry, prevention, compensation, stiffness, and optimization strategies [22]. For positioning stages, the ideal strategy should reduce both rotational and translational deviations. Only a few strategies have the potential to do this. These strategies in combination with known mechanisms could be helpful in the design of straight-line mechanisms in the order of nanometers.

Despite the well-known compliant mechanisms, the accuracy of nanopositioners is rarely discussed. An overview of the available literature can provide the reader a starting point.

The goal of this paper is to create a categorized overview, to find and compare mechanisms that could be suitable for a particular positioning application in combination with strategies to reduce deviations. The condensed results save time for researchers by directing them to the articles that pertain to their work.

The literature study consists of three parts. To create a broad view of the literature, first the compliant straight-line mechanisms retrieved are shown. Second, the state of the art of one degree of freedom nano-positioners are given, including mechanisms that can result in 1-DoF translational positioners. Thereafter, strategies for handling parasitic motions are given.

In section II, relevant background information is given. Thereafter, a search plan and classification method is discussed, in section III. The different types of flexures and mechanisms, together with the state-of-the-art is given in section IV. section V will discuss the results found. The conclusions are presented in section VI.

II. Background

In this chapter, relevant background information is presented for this study.

A. Travel accuracy vs Position accuracy

Any rigid body has six degrees of freedom. These consists of three translations along the perpendicular axes X, Y, and Z, and rotations around these axes. A distinction must be made between travel and positioning accuracy. Travel accuracy is determined along the way from point A to B, where positioning accuracy is the error between the set point and the actual point of positioning.

B. Parasitic motions

The purpose of a one degree of freedom positioner is to translate an object in a perfect straight motion. A parasitic motion is defined as a depended motion which occurs when an independent input motion is given [23]. The parasitic motions occur at the remaining five degrees of freedom, in the case of a Z-motion. The five deviations around the straight line are: translation in the X axis; translation in the Y axis; rotation around the X axis (Yaw, Rx); rotation around the Y axis (Pitch, Ry); and rotation around the Z-axis (Roll, Rz). Pitch and yaw deviations are also known as flatness and straightness errors, respectively. In Figure 1, the used coordinate system and the defined parasitic motions are visualized.

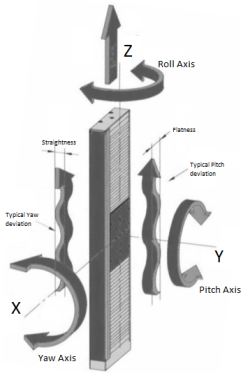

Fig. 1. Definitions of coordinate system [9]

C. Gruebler's Equation

For the analysis of nanopositioners a short introduction should be given to kinematic constraint. Kinematic constraint is concerned with the number of degrees of freedom possessed by a mechanism geometry. If the degree of constraint does not exactly match the required freedom, it is unlikely that the design will function as expected [12]. The equation used to determine if a mechanism is kinematic constraint, under constrained, or over constrained is Gruebler's equation:

$$F = 3(n-1) - 2L - H \tag{1}$$

This equation is valid for two dimensional linkage systems where F is the number of DoF, n the number of links, L the number of lower pairs (one DoF such as pins and sliding joints) and H the number of higher pairs (two DoF such as cam and gear joints) [24]. For spatial mechanism, the degrees of freedom are calculated differently. There are six degrees of freedom in space and three degrees of freedom in a plane for any unconstrained rigid body. The rigid body system's degrees of freedom will decrease in direct proportion to the addition of kinematic constraints between rigid bodies. To determine the degrees of freedom the kinematic constraints per joint are investigated and subtracted from the unconstrained degrees of freedom, according to:

$$F = 6(n-1) - \sum_{i=1}^{J} c_i \tag{2}$$

, where F is the number of DoF, n the number of bodies, J the number of joints, and $\sum c$ the total number of constraints.

D. Approximate vs exact straight-line mechanisms

An exact straight-line mechanism is a mechanical system theoretically (i.e. without any mechanical imperfections) trace an exact straight line, meaning that the output motion of the mechanism is a straight line without any deviation. The straight line is obtained mostly by more than four bar linkages and complex compliant joints, such as a prismatic joint. These mechanisms are usually complex, require precise manufacturing and/or assembly to achieve the desired result.

On the other hand, an approximate straight-line mechanism is a mechanical system that is designed to trace a path that is very close to a straight line, but not necessarily perfectly straight. These mechanisms often utilize four bar linkages. These mechanisms are usually simpler and less precise than exact straight-line mechanisms. However, they are easier to design and manufacture, which could lead to less imperfections that results in better performance than exact straight-line mechanisms, in practice.

III. Method

A. Search Method

To retrieve all relevant literature related to nanopositioners a search plan is made. The stage is described within several subjects: Compliant Mechanisms, Translation Stage, Precision Engineering, and Parasitic Motion. Keywords and their synonyms, gradually complemented, related to these subjects are used into SCOPUS. Papers were stored based on their abstract and pictures. These papers are reviewed and also their references are used to obtain relevant literature. The keywords used can be found in Table I together with the average of the number of document results. The keywords are inserted from top to bottom, resulting in eventually combinations of four keywords and the number of result documents. This, to show how the literature is becoming more and more specific per keyword. For instance, the search string: (TITLE-ABS-KEY(compliant) AND TITLE-ABS-KEY(linear) AND TITLE-ABS-KEY(nano) AND TITLE-ABS-KEY(error)); gives 22 results.

B. Classification

To compare the found literature, a classification will be made. The categories and criteria used for nanopositioners are found along the way of reading literature.

First, the found flexures and mechanisms are described. The flexures will be sorted into overarching groups. The mechanisms will be sorted based on geometry: planar, spatial, or out-of-plane planar mechanisms, and if they are or approximate an exact straight line.

The first category to create groups is the distinction between spatial, planar, and out-of-plane planar geometries. Spatial geometries includes geometries in the 3D-coordinate system. The flexible elements are not in-plane with the motion. Opposite to spatial geometries are the planar geometries where the flexible elements are in-plane with the motion. A last distinction is made for out-of-plane planar geometries. These geometries have an in-plane geometry but an out-of-plane motion, they are referred to orthoplanar springs.

Several criteria are set to create an overview. Multiple criteria are dependent on the flexure and mechanism geometry to visualize the stages, and the other criteria are based on the performance. Firstly, different types of flexures are investigated. Secondly, common rigid-body-links are found in the literature and is used as a visualization criterion. The last visualization criterion are the dimensions.

To sort the literature based on performance, the stroke and the parasitic motions are obtained from the literature. These criteria represent the most critical requirements based on performance. These can be combined with each other and with the building volume, leading to several ratios. The ratios that are assumed relevant are between each individual parasitic motion and stroke, Δx/s Δy/s, Δz/s, $\Delta\theta_x$/s, $\Delta\theta_y$/s, $\Delta\theta_z$/s, and the ratio between the dimension in drive direction and stroke, s/L_z. There are two assumptions made for these ratios: 1) The parasitic motion is linear to the stroke ; 2) The dimension in drive direction is minimized. These ratios give insight how the found literature relate to one another.

IV. Results

First, a distinction was made about the type of flexure and mechanism. Second, an overview of the found literature is given. Thereafter, the highlights of the found literature will be briefly reported. Lastly, suitable parasitic motion strategies are shown and linked to the literature.

A. Type of flexures

Different types of flexures are observed during the literature study. These are briefly described and shown.

Leaf springs

Flexures where the flexibility is distributed equally over the entire flexible element, are referred as leaf springs. These springs have a constant cross-section, resulting in a distributed stress concentration. A leaf spring has three degrees of freedom, one translation and two rotations. In Figure 2, an illustration of a leaf spring is shown. A disadvantage of these springs is there reduction in support stiffness when curved [26].

Notches

There are many types of a notch profile, such as rectangular corner-filleted, circular, parabolic, and spherical section. In the literature, three notch-types are found: the rectangular corner-filleted, the circular, and the parabolic profiled notch. These notches bend only in one degree of freedom and are shown in Figure 2. The notches have lumped compliance, meaning that the flexion concentrates itself in a small region close to the notch, causing high stress concentrations in the mechanism [27].

Rotational joints

Compliant rotational joints are designed to create a pure rotational motion [25]. The two rotational joints used in the found literature is the compliant cartwheel joint, and two cartwheel joint in series, referred to a X2 joint, shown in Figure 2. The rotation axis of these joints deviates according to the rotational motion causing small errors and/or internal stresses.

TABLE I
USED KEYWORDS AND THE NUMBER OF RESULT DOCUMENTS

Subject	Keywords	No. documents
Compliant Mechanism	Monolithic, Flexure, Compliant, Lumped, Flexible, Elastic	100000
Translational Stage	One-axis, Single-axis, One degree of freedom, (Recti)linear, Straight, Guidance, Stage	1000
Precision Engineering	Precision, Accurate, (Sub)nano, nano positioning, Positioning	100
Parasitic motion	Parasitic, Ultra-linear, Error, Trajectory, Tracking	20

TABLE II
SORTED TYPE OF MECHANISM

-	Exact Straight-Line	Approximate Straight-Line
Planar Mechanism	Peaucellier Double parallelogram	Watt's Linkage Roberts Linkage Scott-Russel Mechanism Roberts-Chebyshev Mechanism Single parallelogram 13-Hinge Mechanism
Spatial Mechanism	Sarrus mechanism Six folded leaf spring	-
Out-of-plane planar mechanism	Howell's Ortho-planar spring	-

Folded leaf springs

Folded leaf springs constrains one degree of freedom, the translational degree of freedom in the direction of the folding line. The stiffness of these springs is determined by the shear stiffness of the leaf spring, see Figure 2.

B. Type of mechanisms

An overview representation of the straight-line mechanisms found are shown in Table II, the table with schematic representations can be found in Appendix A. The mechanisms that are found as nanopositioners consist of parallelograms or is a six folded leaf spring mechanism.

C. Found Literature

If we focus, in literature, on straight-line mechanisms that are suitable as a nano-positioner, only a few references are left. The references that are left, either discussed information that can be relevant for nano-positioners or came close to nanometer accuracy. The application, flexure types, mechanism type, performances, and the way of measuring is described, if known. An overview of the results of the high accuracy mechanisms is shown in Table III.

Spatial 1-DoF Mechanisms

Koster et al. have developed ARCADE. It is a calibration device of GRADIO, which is the core instrument of the Aristoteles satellite [28]. GRADIO measures the Earth gravity field. The mechanism is based on a 13-hinge mechanism. However, the lever that is needed for such a mechanism is not favorable in terms of compactness. They have created a more compact design but is overconstrained, and allows relatively small deflections. The mechanism consists of three monolithic planar mechanisms, symmetrical placed around 120 degrees, which together create a large spatial design of 200x200x200mm. The mechanism consists of two types of flexible elements, rectangular corner-filleted notches and circular notches in combination with a rigid body the maximal flexure length is 100mm. Along a stroke of 5mm, ARCADE deviates along axes X and Y two with 15nm and rotates around these axes with 5µrad.

Cosandier et al. created a translational stage for the watt balance [17][29]. The watt balance is a promising way to link the kilogram to the Planck constant. A decisive part is the linear stage. Cosandier et al. designed a monolithic 13-hinged mechanism. The mechanism consists of a double parallelogram. The maximal length of the flexible elements is 200mm. Two types of flexible elements are seen: rectangular corner-filleted notches with an intermediate rigid body and a rotational X2

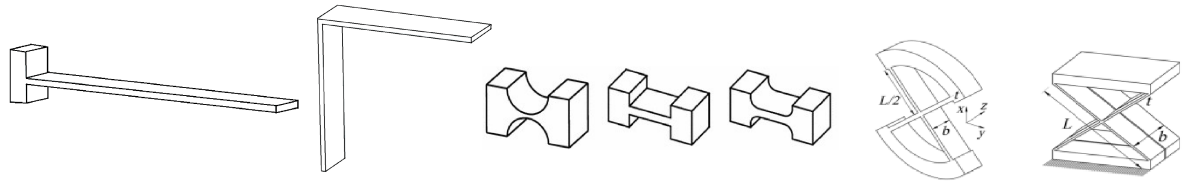

Fig. 2. Type of flexure: Leaf spring, folded leaf spring, circular notch, rectangular corner-filleted notch, parabolic profiled notch, cartwheel joint , X2 joint [25]

joint. To create a static determined mechanism, they have added a lever with a ratio of 1:2. The results along a 40mm stroke are impressive. The mechanism deviates 180nm and 40nm along the axes X and Y, respectively, where rotations did not get larger than 5.3 µrad around the Y axis, and even 3µrad around the X axis.

Together with the 13-hinge mechanism, they have designed an assembled Sarrus guide, with dimensions 290mm x 290mm x 150mm. The Sarrus guide consists of two single parallelograms placed perpendicular to each other consisting of three rectangular corner-filleted notches creating a crossed bldes pivot point. The parasitic motions are promising along the stroke of 40mm. Translational deviations along the X and Y-axis are 200nm and 500nm, respectively. While the rotations are around X and Y are 275µrad and 220µrad, respectively. Cosandier et al. measured their performance making use of a SIOS interferometer with 0.1nm resolution to measure lateral positions and an autocollimator to measure the angular deviation.

The mechanism designed by Haitjema et al. is worth mentioning, while VDL have designed such a system [30][31]. The mechanism consists of six folded leaf springs symmetrically placed around a cylindrical tube in two layers, three springs at the top and three springs at the bottom of the tube. The design is large in height to create certain tip/tilt stiffness. Haitjema et al. only mentioned their stick/slip accuracy of 0.2nm and a $\Delta\theta_y$ of 3nm. The results obtained by VDL are more extensive. The mechanism, with a diameter of 195mm and a height of 115mm, has a stroke of 100μm. Over this stroke, a parasitic translation of 5nm along the X and Y axes is measured. Furthermore, the mechanisms rolls around the Z-axis with 300nrad. The measured yaw and pitch were 6700nrad and 800nrad, respectively. The measurment equipment used are interferometers with a resolution of 10 nm.

Planar 1-DoF Mechanisms

Duarte et al. built a rectilinear-motion machine based on flexural principles for X-ray spectrometry purposes [32]. The design has a linear motion of 15mm and is made monolithically. It is based on the double parallelogram principle, they used rotational cartwheel joints as pivot points. Their focus was on the tilt angle. Therefore, only this result is given and deviates with 1.8 µrad.

Smith et al. designed a monolithic spring mechanism based on a symmetric 100x100mm double parallelogram [33]. The flexible elements consist of circular notches that allow a rotational motion. Their design allowed a horizontal displacement of 0.05mm. The mechanism deviated with 5nm and 4000nm along the X and Y-axis, respectively, measured with a laser measurement system which exhibited a realisable accuracy of 50nm. Furthermore, they measured a pitch error of 250nrad with a two-dimensional autocollimator.

A bench was set up for calibration of line scale standards by optical microscopy by Pousset et al. [34]. Part of the bench was a linear table. It is based on a double parallelogram with parabolic profiled notches as flexible elements. Along a stroke of 24mm, the mechanism is designed with a maximal parasitic motion of $1\mu m$ in the translational directions. The allowable parasitic rotation is below $100\mu rad$.

A linear in-plane motion up to 200 µm was allowed by the translation stage of Becker et al. [35]. The design is a symmetrical double parallelogram consisting of circular notches, and manufactured monolithically. They claim a smooth translation within one hundredth of a nanometer, and tilts below 1 nrad over the full range of motion. In order to reduce the parasitic motions, they have added additional torques in proportion to the displacement in the form of magnets. The rotations are measured with a autocollimator.

The mechanism of Jones et al. consists of four pairs of leaf springs [36]. These pairs created a mechanism based on a symmetric single parallelogram. Along a 10mm stroke, it deviates with 2000nm and 500nm in X and Y direction. The measured parasitic rotations were $10\mu rad$, $63\mu rad$, and $136\mu rad$ as yaw, pitch, roll, respectively.

The article of Alemanni et al. describes the basic criteria for the translation system design for x-ray interferometric scanning [37]. They have designed a single monolithic parallelogram consisting of four parabolic profiled notches. A rotation of 3.6 μrad around the X-axis was measured with an autocollimator along a 0.13mm stroke. The autocollimator had a sensitivity of 0.28 μrad.

Tissot-Daguette et al. proposed a new design on a single parallelogram [38]. Instead of using individual leaf springs, they used these springs to create Remote

Center of Compliance pivots. By doing this, a maximum parasitic translation of 65.6 nm was observed in the FEA along a stroke of 8mm. The occurring parasitic roll motion was 13.6 µrad.

Out-of-plane 1-DoF Mechanism

Chen et al. designed and optimized a out-of-plane 1-DoF mechanism, referred as orthoplanar flexure [39]. They have maximized the ratio of the radial stiffness to the out-of-plane drive stiffness. The geometry has a radial pattern and had a diameter of 200mm and a height of 35mm. Moving 0.14mm, t hey observed 2000nm deviation along the X and Y axis. Around the X and Y axis a rotation of 26μrad was observed.

The patent of Howell et al. [40] is included in the results because of their design is a new approach to rectilinear movement. Their design is an ortho-planar spring. It is a rotational symmetric double parallelogram design around 120°. The design has the ability to create a relatively large stroke regardless of their small volume. However, the results regarding parasitic motion have to be seen in future.

D. Parasitic Motion Strategies

Parasitic strategies are discussed extensively by Meinders [22]. There are only a few strategies that are suitable for positioning stages, while a suitable strategy should have the ability to compensate both, rotational and translational deviations, in a continuous way. The possible strategies found by Meinders will be briefly described and linked to the literature of nanopositioners.

Maximize the degree of symmetry

A well-known method to reduce parasitic motion is to maximize the degree of symmetry. The degree of symmetry is the amount of perpendicular symmetry planes a mechanism has. [32][35][33][39][41][40] used this method to reduce parasitic motion in their 1-DoF stages.

Make use of rotational symmetry

In line with previous strategy, this method is also based on symmetry. This time on rotational symmetry. Du studied the influence of rotational symmetry for planar mechanisms [42]. It turned out that a multiple of 2 or 3 symmetry axes around the end effector resulted in a diagonal stiffness matrix, and is thus free of parasitic motions at its center point, [28][30][41][40] are found examples.

Compensate with module in series

This strategy adds a module to the mechanism with the same parasitic motions but than in opposite direction. By doing this the parasitic motions eliminate each other and creates a perfect motion. This method is well-known in literature in the form of the double parallelogram mechanisms [29][32][34][33], which are described earlier.

Compensate within the mechanism

This method aims on the parasitic motion within the

TABLE III
CLASSIFICATION OF THE COMPLIANT 1-DOF STAGES

		Flexure Type					Mechanism Type						# of flexible elements	Dimensions [mm]			Stroke [mm]	Parasitic Motion [nm, nrad]					
	Ref.	Leaf Spring	Rectangular corner-filleted notch	Notch	Rotational joint	Folded leaf spring	Single parallelogram	Double parallelogram	Symmetric parallelogram	Six folded leaf springs	Overconstrained	Monolithic		X	Y	Z		Δ X	Δ Y	Δ Z	$\Delta\theta_X$	$\Delta\theta_Y$	$\Delta\theta_Z$
Spatial Mechanism	[28]		●	●				●	●		●	◐	16	200	200	200	6	15	15	-	5000	5000	-
	[29]		●		●			●				●	13	140	350	450	40	180	40	-	9000	5300	-
	[29]		●		●		●				●		32	290	290	150	40	200	500	-	275000	220000	-
	[30]					●				●	●		6	-	-	-	0.015	-	-	0.2	-	3	-
	[31]					●				●	●		6	195	195	115	0.1	5	5	-	6700	800	300
Planar Mechanism	[32]				●			●	●		●	●	16	-	300	300	15	-	-	0.8	-	1800	-
	[33]			●				●	●		●	●	16	-	100	100	0.05	5	4000	-	-	250	-
	[34]			●				●				●	8	-	300	300	24	1000	1000	1000	100000	100000	100000
	[35]			●				●	●		●	●	16	-	200	200	0.2	few	few	-	0.32	0.32	-
	[36]	●					●		●		●		8	100	25	75	10	2000	500	-	10000	63000	136000
	[37]			●			●				●	●	4	-	100	100	0.13	-	-	-	3600	-	-
	[38]	●					●				●	●	8	20	135	175	8	65.6	-	-	-	13600	-
Out-of-Plane Planar Mechanism	[39]	●						●	●		●	◐	-	200	200	35	0.14	2000	2000	-	26000	26000	-
	[40][41]	●						●			●	●	-	-	-	-	-	-	-	-	-	-	-

joints. For instance, most compliant rotational joints experience a shift of center of rotation causing parasitic motion. If during the motion this shift can be compensated, the parasitic motions are reduced. This strategy is unknown, to the best of authors knowledge, in the found literature of nanopositioners.

Optimize the joints

As the above strategy, this method also focuses itself on the joints. However, in this case the joints are theoretical optimized for a parasitic motion free motion. There are several methods to optimize a joint, for instance topology or shape optimization. Chen et al. used shape optimization for their design [39].

V. Discussion

The results found will be discussed. First of all, there should be mentioned that literature about compliant nanopositioners and their parasitic motion is scarce. As the keywords string became more specific in SCOPUS less literature was found. This could be the result of control systems. The behavior of the one DoF nanopositioners found in this review relies completely on the mechanics, while nowadays the systems transformed to mechatronic systems where the mechanics are controlled. Furthermore, the literature found never gave full information about all parasitic motions. Most studies focused itself on chosen degrees of freedom instead of all six. Interesting to see is that their are only three articles that measured and mentioned the parasitic roll motion. All exact straight-line mechanisms or a variation on that are used, except the Peaucellier linkage. It is challenging to compare the literature because of the many variations. Nevertheless, an overview was created and tentative conclusions can be made. The visualisation of the discussed mechanisms can be found in Appendix B.

Koster et al. reached to smallest ratio Δx/s=2.5, they created a mechanism that deviates along the x-axis with 2.5nm per millimeter over a 6mm stroke [28]. It is worth mentioning that the Sarrus guide and the 13-Hinge mechanism of Cosandier et al. came close, Δx/s=5 and Δx/s=4.5[17][29]. Compared to Koster et al. they have managed to reached this along a 40mm stroke.

Further, the 13-hinge mechanism Cosandier et al. developed has the smallest parasitic motion ratio in one direction, Δy/s=1, and $\Delta\theta_x$/s=225. They used a double parallelogram principle that fits the *Compensate with module in series* strategy. Resulting in a minimization of the deviation along the y-axis along the 40mm stroke.

Becker et al. reached the smallest $\Delta\theta_y/s = 1.6$ and $\Delta\theta_z/s = 1.6$ ratio. However, their mechanism is not fully based on mechanics. They made use of magnetic tilt compensation elements.

It is noteworthy that the Sarrus guide of Cosandier et al. have the highest s/L_z ratio, 0.2667, suggesting that mechanisms of this type could be beneficial when the dimension in drive direction is limited.

An interesting result can be seen when the maximum ratio of parasitic translation and the stroke/volume ratio

TABLE IV
Overview of the results of the compliant 1-DoF stages

		Relative parasitic motion [nm/mm]						Height/Stroke [mm/mm]
	Ref.	Δx/s	Δy/s	Δz/s	$\Delta\theta_x$/s	$\Delta\theta_y$/s	$\Delta\theta_z$/s	s/L_z
Spatial Mechanism	[28]	2.5	2.5	-	833	833	-	0.03
	[29]	4.5	1		225	132.5	-	0.0889
	[29]	5	12.5	-	6875	5500	-	0.2667
	[30]	-	-	0.2	-	3	-	-
	[31]	50	50	-	67000	8000	3000	0.0009
Planar Mechanism	[32]	-	-	0.0533	-	120	-	0.05
	[33]	-	80000	-	-	5000	-	0.0005
	[34]	41.67	41.67	41.67	4166.67	4166.67	4166.67	0.08
	[35]	-	-	-	-	1.6	1.6	0.001
	[36]	200	50	-	1000	6300	13600	0.1333
	[37]	-	-	-	423.1	-	-	0.0013
	[38]	8.2	-	-	-	1700	-	0.0457
Out-of-Plane Planar Mechanism	[39]	14285.7	14285.7	-	185714	185714	-	0.004
	[40][41]	-	-	-	-	-	-	-

are combined, $max(\Delta x/s; \Delta y/s)/(s/L_z)$. This combined ratio should be minimized, while the parasitic motion and the dimension in drive direction should be minimized and the stroke maximized. The difference between spatial and planar mechanisms is significantly. The spatial mechanisms taken on average have a smaller ratio than the planar mechanism, suggesting that spatial mechanisms are more beneficial as a nanopositioner. On the other hand, the complexity is increased in these mechanisms.

It is hard to compare between the spatial mechanisms while they make use of multiple types of flexure. The influence of each flexure individually in a mechanism to the performance is out of scope. Therefore, there is no clear relation between flexure type and the defined ratios within spatial mechanisms. Planar mechanisms did make use of only one type of flexure within a mechanism. Unfortunately, there is no clear relation found between the flexure type and ratios. However, there are some interesting comparisons between some articles.

It is interesting to compare the 13-hinge mechanism of Koster et al. and Cosandier et al. while they have similarities[28][29]. Both are based on the same principle, only Koster et al. wanted to create a more compact design. The design of Koster et al. is overconstrained and symmetric unlike the design of Cosandier et al.. The maximum flexure length of Cosandier et al. is twice as long as the Koster et al. design, suggesting the range of motion will be twice as long. In theory, the design of Koster et al. should have a smaller range of motion due to the symmetry. The symmetric design have parasitic motions in opposite directions resulting in a smaller parasitic motions but also a loss in range of motion, which agrees to the found literature in Table III.

If we compare Becker et al. and Jones, their similarities lie in their mechanism type, both are an overconstrained symmetric single parallelogram mechanism [35][36]. However, Becker et al. used notches as flexible elements and Jones used leaf springs. Theory tells us that leaf springs have a distributed compliance, resulting in smaller stresses and a larger range of motion compared to the lumped compliance of notches. The flexures of Becker et al. are more than twice as long as the flexures of Jones. However, the range motion is 50 times smaller, suggesting that the leaf springs indeed have a larger range of motion. Disadvantage to the use of leaf springs is that their support stiffness reduces when curved.

More generally, from the results it appears that twelve out of fourteen have a mechanism type consisting of a single parallelogram or a double parallelogram.

Two mechanisms are not overconstrained. Interesting to see is that these mechanisms have a significant larger range of motion compared to the others, an exemption is the Sarrus guide of Cosandier et al. [29].

The results show that all planar mechanisms are made monolithic except of the mechanism of Jones et al. [36]. Furthermore, most of the spatial mechanisms were created non-monolithically.

Worth mentioning is the patent of Howell et al. [40]. This design uses three beneficial strategies to reduce parasitic motion. Their design is symmetric and compensates with module in series. Three double parallelogram mechanisms are placed each at 120°. Presumably, if this design was measured, the ratio s/L_z would be relatively large, due to their out-of-plane motion. However, only one application has been found for orthoplanar springs. Chen et al. designed such a spring for a linear motion and their stroke/volume ratio was not large compared to other designs [39]. Nonetheless, their design is the smallest in the drive direction.

A big remark that should be considered relevant to measuring with nano-accuracy is determining what is actually measured. The main issue of the found literature that if they discuss their way of measuring, there are still many unknowns. For instance, the articles that discusses measuring with interferometers did not describe the conditions of the surroundings. As known, interferometers are sensitive to temperature and humidity. Therefore, the conditions must be mentioned to have a better insight in what is actually measured. Another unknown is the mirror alignment, the mirror surface should be placed perpendicular to the interferometer. A small variation could lead to a linear measurement error, because the misalignment will be measured instead of the travel accuracy.

VI. Conclusions

First, existing straight-line mechanisms are mentioned. Thereafter, an overview of the available literature related to compliant one degree of freedom nanopositioners has been made. The highlights of each positioner is

briefly described, and eventually compared to each other. Certain strategies that are suitable for positioners are given, and related to the existing nanopositioners.

It was found that different type of flexures and mechanism types are used. From the results, no clear relation is found between the type of flexure and their performance regarding parasitic motion. From the comparison between Becker et al. and Jones [35][36], a tentative conclusion can be taken related to the flexure type. Namely, leaf springs have a larger stroke than flexures consisting of notches.

There are multiple mechanisms that achieve or approach a straight-line. However, the existing literature in nanopositioning only consists of a few mechanisms. Future research should be done on the use of other straight-line mechanisms as the foundation of nanopositioners, for instance a Peaucellier linkage.

The ratios gave insight about the existing literature. The Sarrus guide of Cosandier et al. had the largest stroke/volume ratio, $s/L_z = 0.2667$. The 13-hinge mechanism of Cosandier et al. has the largest stroke, 40mm, and the smallest ratio related to translational parasitic motion, $\Delta y/s = 1$. Furthermore, Becker et al. has the smallest ratios related to rotational parasitic motion, $\Delta\theta_y/s = 1.6$ and $\Delta\theta_z/s = 1.6$. However, they have used compensating magnets to achieve this. A combination of the stroke/volume ratio and the largest ratio related to translational parasitic motion showed that spatial mechanisms have a smaller combined ratio than the planar mechanisms.

It seems that if the design is perfectly constrained-, in this case one DoF and no overconstraints (i.e. $F = 1$), it would be beneficial for the range of motion.

It is shown that the literature available about compliant 1-DoF nanopositioners is scarce. There is no compliant 1-DoF nanopositioner available where all the parasitic motions are given. Furthermore, there is no literature that extensively describes how to measure these motions in the order of nanometers.

A promising direction for future research would be to find a well-constrained compact design that maximizes the use of parasitic motion strategies to minimize the parasitic motion to nanometers, and measures these in all directions.

REFERENCES

[1] B. Choi, S. Sreenivasan, S. Johnson, M. Colburn, and C. Wilson, "Design of orientation stages for step and flash imprint lithography," *Precision Engineering*, vol. 25, no. 3, pp. 192–199, 2001.

[2] J. Lee, K.-B. Choi, and G.-H. Kim, "Design and analysis of the single-step nanoimprinting lithography equipment for sub-100 nm linewidth," *Current Applied Physics*, vol. 6, no. 6, pp. 1007–1011, 2006.

[3] J. Park and W. Moon, "An xy scanner with minimized coupling motions for the high speed afm," in *Proceedings of the Korean Society of Precision Engineering Conference*, Korean Society for Precision Engineering, 2005, pp. 653–656.

[4] D. Kim, D. Y. Lee, and D. G. Gweon, "A new nano-accuracy afm system for minimizing abbe errors and the evaluation of its measuring uncertainty," *Ultramicroscopy*, vol. 107, no. 4-5, pp. 322–328, 2007.

[5] R. van der Maas, A. van der Maas, J. Dries, and B. de Jager, "Efficient nonparametric identification for high-precision motion systems: A practical comparison based on a medical x-ray system," *Control Engineering Practice*, vol. 56, pp. 75–85, 2016.

[6] D. M. Brouwer, B. De Jong, and H. Soemers, "Design and modeling of a six dofs mems-based precision manipulator," *Precision Engineering*, vol. 34, no. 2, pp. 307–319, 2010.

[7] J. J. Gorman, Y.-S. Kim, and N. G. Dagalakis, "Control of mems nanopositioners with nano-scale resolution," in *ASME International Mechanical Engineering Congress and Exposition*, vol. 47756, 2006, pp. 151–159.

[8] C. G. Willson and B. J. Roman, *The future of lithography: Sematech litho forum 2008*, 2008.

[9] [Online]. Available: https://www.pi-usa.us/en/tech-blog/straightness-and-flatness-of-air-bearings.

[10] G. J. P. Nijsse, "Linear motion systems: A modular approach for improved straightness performance.," 2002.

[11] M. Reck, "All positioning stages are not created equal," *DSPE MIKRONIEK*, vol. 58, no. 2, pp. 20–

23, 2018. [Online]. Available: https://www.dspe.nl/wp-content/uploads/2018/02/Mikroniek-Issue-2-2018.pdf.

[12] S. T. Smith, *Foundations of ultra-precision mechanism design*. CRC Press, 2003, vol. 2.

[13] J. A. Gallego and J. Herder, "Synthesis methods in compliant mechanisms: An overview," in *International Design Engineering Technical Conferences and Computers and Information in Engineering Conference*, vol. 49040, 2009, pp. 193–214.

[14] G. Radaelli and J. Herder, "A monolithic compliant large-range gravity balancer," *Mechanism and Machine Theory*, vol. 102, pp. 55–67, 2016.

[15] S. Wan and Q. Xu, "Design and analysis of a new compliant xy micropositioning stage based on roberts mechanism," *Mechanism and Machine Theory*, vol. 95, pp. 125–139, 2016.

[16] J. Hricko and S. Havlik, "Design of the 2 dof compliant positioning device based on the straight-line watt's mechanisms," in *Mechanism Design for Robotics: MEDER 2021*, Springer, 2021, pp. 247–255.

[17] F. Cosandier, "Conception d'axes motorisés rectilignes d'ultra-haute précision," EPFL, Tech. Rep., 2013.

[18] Y. Tian, B. Shirinzadeh, D. Zhang, and G. Alici, "Development and dynamic modelling of a flexure-based scott–russell mechanism for nano-manipulation," *Mechanical Systems and Signal Processing*, vol. 23, no. 3, pp. 957–978, 2009.

[19] J. Zhu and G. Hao, "Design and test of a compact compliant gripper using the scott–russell mechanism," *Archives of Civil and Mechanical Engineering*, vol. 20, pp. 1–12, 2020.

[20] D. Stojiljković, N. T. Pavlović, and M. Milošević, "Design of compliant mechanism for rectilinear guiding with non-conventional optimization of flexure hinges," in *Advances in Asian Mechanism and Machine Science: Proceedings of IFToMM Asian MMS 2021 6*, Springer, 2022, pp. 370–378.

[21] J. Hricko, "Conversion of peaucellier-lipkin straight-line mechanism to compact compliant device," *Int. J. Mech. Control*, vol. 16, no. 1, pp. 31–38, 2015.

[22] N. Meinders, "Compensating parasitic motions and cross-couplings in compliant mechanisms: The development of a new compensation strategy to diminish unwanted motions," 2021.

[23] R. Lin, W. Guo, and F. Gao, "On parasitic motion of parallel mechanisms," in *International Design Engineering Technical Conferences and Computers and Information in Engineering Conference*, American Society of Mechanical Engineers, vol. 50169, 2016, V05BT07A077.

[24] D. H. Myszka, *Machines and mechanisms*. Prentice Hall, 2004.

[25] D. Farhadi Machekposhti, N. Tolou, and J. Herder, "A review on compliant joints and rigid-body constant velocity universal joints toward the design of compliant homokinetic couplings," *Journal of Mechanical Design*, vol. 137, no. 3, p. 032 301, 2015.

[26] D. M. Brouwer, J. P. Meijaard, and J. B. Jonker, "Large deflection stiffness analysis of parallel prismatic leaf-spring flexures," *Precision engineering*, vol. 37, no. 3, pp. 505–521, 2013.

[27] A. Dunning, "Design of a zero stiffness six degrees of freedom compliant precision stage," 2011.

[28] M. P. Koster, "Constructies voor het nauwkeurig bewegen en positioneren," *Mikroniek*, vol. 34, no. 2, pp. 38–42, 1994. DOI: https://www.dspe.nl/wp-content/uploads/1994/02/Mikroniek-Issue-2-1994.pdf.

[29] F. Cosandier, A. Eichenberger, H. Baumann, *et al.*, "Development and integration of high straightness flexure guiding mechanisms dedicated to the metas watt balance mark ii," *Metrologia*, vol. 51, no. 2, S88, 2014.

[30] H. Haitjema, N. Rosielle, G. Kotte, and H. Steijaert, "Design and calibration of a parallel-moving displacement generator for nano-metrology," *Measurement Science and Technology*, vol. 9, no. 7, p. 1098, 1998.

[31] E. de Groot, "022376/aa," VDL ETG T&D, Tech. Rep., 2023.

[32] R. Duarte, M. R. Howells, Z. Hussain, T. Lauritzen, and R. McGill, "A linear motion machine for soft x-ray interferometry," Lawrence Berke-

ley National Lab.(LBNL), Berkeley, CA (United States), Tech. Rep., 1997.

[33] S. Smith, D. Chetwynd, and D. Bowen, "Design and assessment of monolithic high precision translation mechanisms," *Journal of Physics E: Scientific Instruments*, vol. 20, no. 8, p. 977, 1987.

[34] N. POUSSET, J. SALGADO, and G.-P. VAILLEAU, "Étalonnage de micromètres objets par microscopie optique calibration of line scale standards by optical microscopy,"

[35] P. Becker, P. Seyfried, and H. Siegert, "Translation stage for a scanning x-ray optical interferometer," *Review of scientific instruments*, vol. 58, no. 2, pp. 207–211, 1987.

[36] R. Jones, "Parallel and rectilinear spring movements," *Journal of Scientific Instruments*, vol. 28, no. 2, p. 38, 1951.

[37] M. Alemanni, G. Mana, G. Pedrotti, P. Strona, and G. Zosi, "On the construction of a zerodur translation device for x-ray interferometric scanning," *Metrologia*, vol. 22, no. 1, p. 55, 1986.

[38] L. B. Tissot-Daguette, H. P.-M. B. Schneegans, Q. Gubler, C. Baur, and S. Henein, "Rectilinear translation four-bar flexure mechanism based on four remote center compliance pivots," in *Proceedings of the 22nd International Conference of the European Society for Precision Engineering and Nanotechnology*, euspen, 2022.

[39] S.-C. Chen, D. Golda, A. Herrmann, and A. H. Slocum, "Design of an ultra precision diaphragm flexure stage for out-of-plane motion guidance," in *International Design Engineering Technical Conferences and Computers and Information in Engineering Conference*, vol. 46954, 2004, pp. 1015–1021.

[40] L. L. Howell, S. Thomson, J. A. Briscoe, *et al.*, "Compliant, ortho-planar, linear motion spring," US6983924B2, Jan. 2023.

[41] J. J. Parise, L. L. Howell, and S. P. Magleby, "Ortho-planar linear-motion springs," *Mechanism and machine theory*, vol. 36, no. 11-12, pp. 1281–1299, 2001.

[42] Y. Du, T. Li, Y. Jiang, and J. Zhang, "Output decoupling property of planar flexure-based compliant mechanisms with symmetric configuration," *Mechanical Sciences*, vol. 7, no. 1, pp. 49–59, 2016.

APPENDIX

Cont.

Appendix A

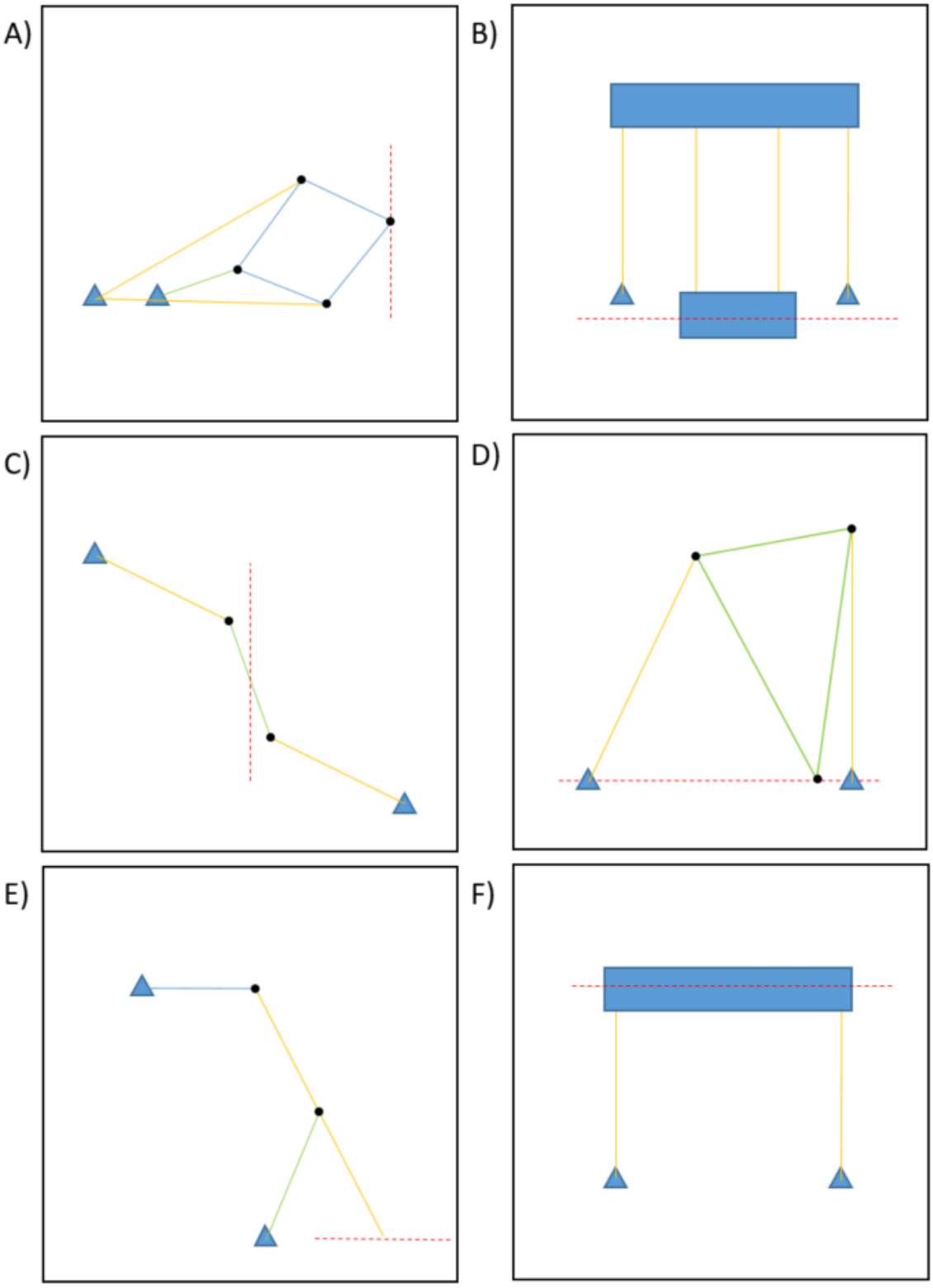

G)

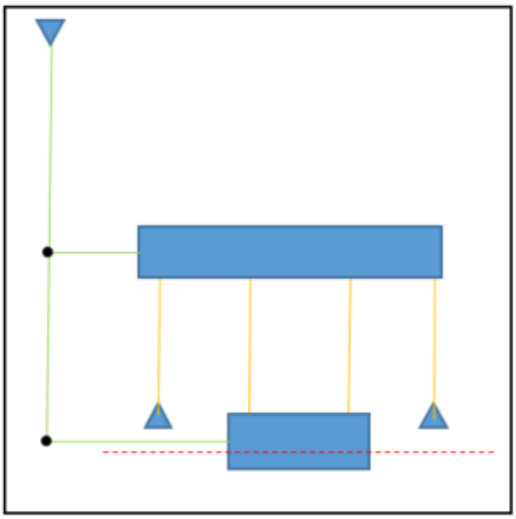

H)

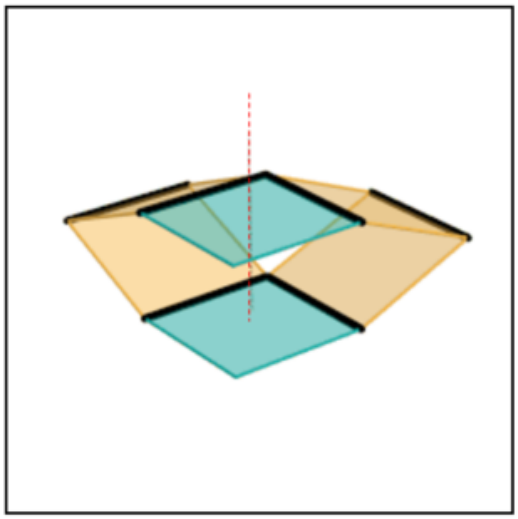

I)

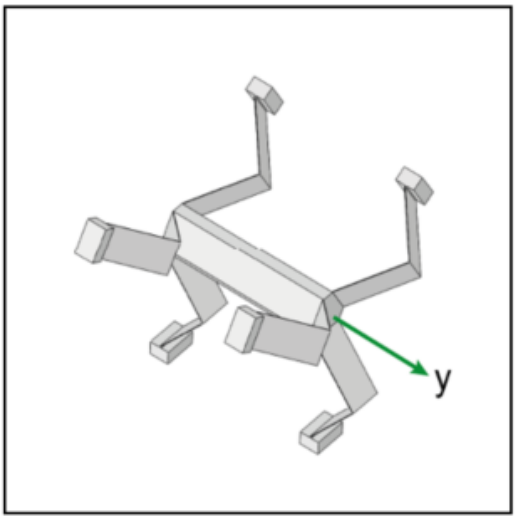
y

J)

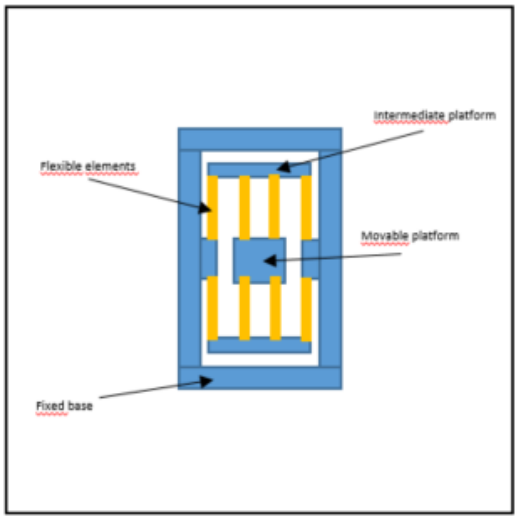
Intermediate platform
Flexible elements
Movable platform
Fixed base

Appendix B

A)

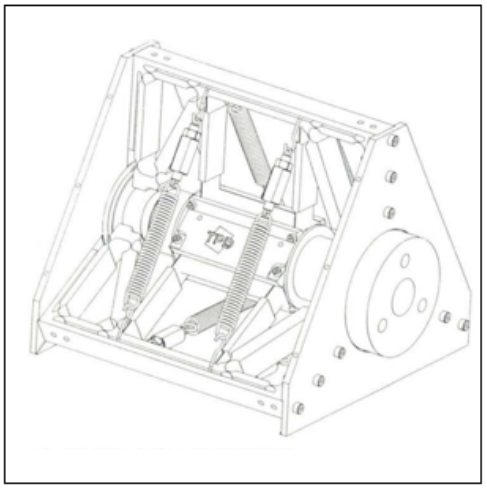

B)

C)

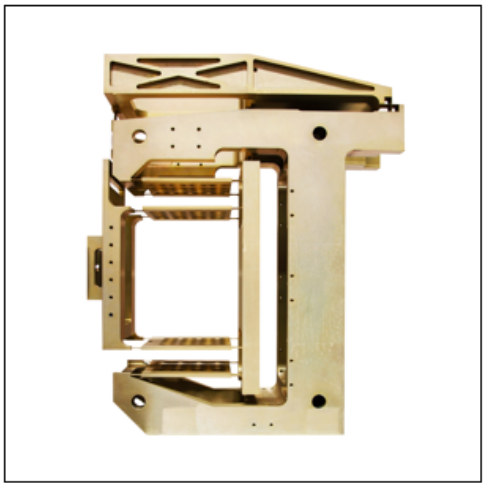

D)

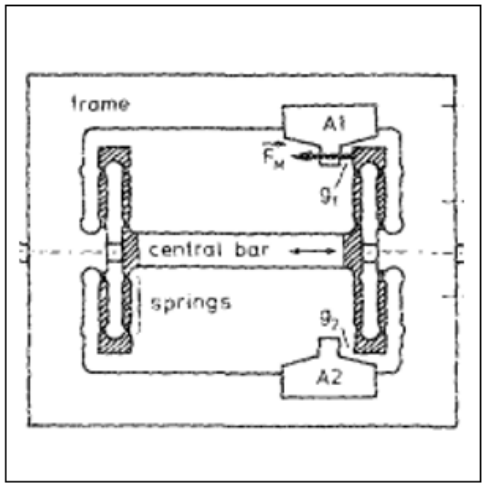

E)

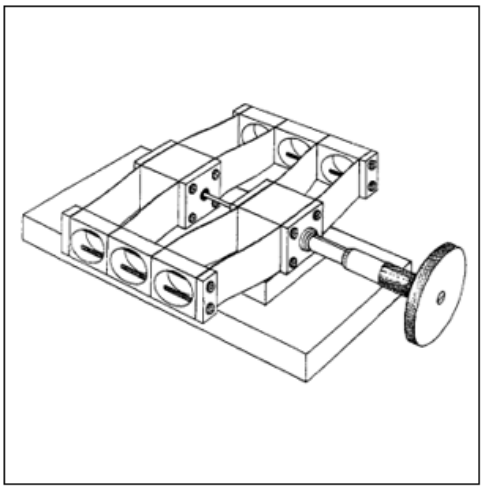

F)

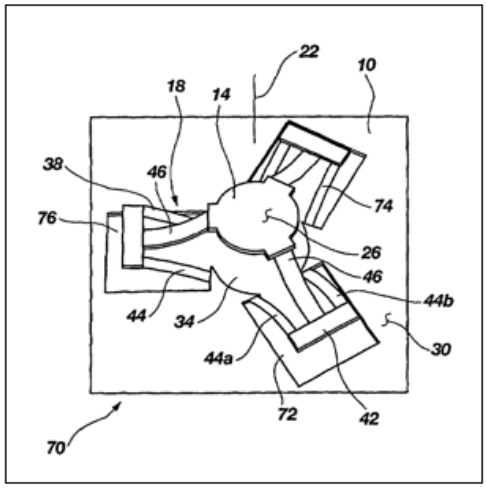

G)

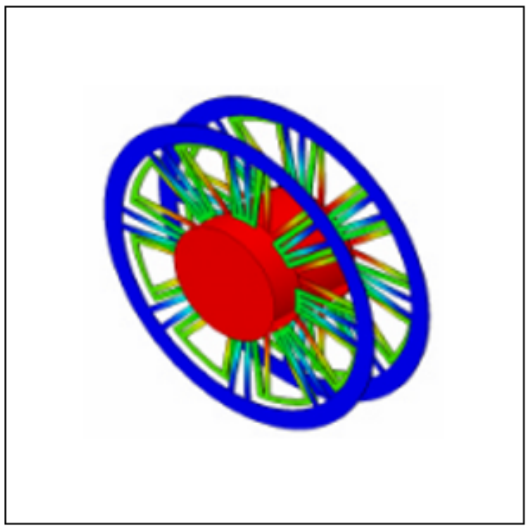

A) Koster et al. (1994) [28] ;B) Cosandier et al. (2013) [17]; C) Cosandier et al. (2014) [29]; D) Becker et al. (1987) [35]; E) Jones et al. (1951) [36]; F) Howell et al. (2023) [40]; G) Chen et al. (2004) [39]

2

Research Paper

A Compact Ultra-Linear Compliant Torsion Reinforced Sarrus Mechanism

Joran L. van Velden[a]

[a]*Delft University of Technology , Mekelweg 5, Delft, 2628 CD, Zuid-Holland, The Netherlands*

Abstract

In this study, a promising design for a compact, ultra-linear Compliant Torsion Reinforced Sarrus mechanism (CORS), capable of achieving ultra-linear motion is presented. The CORS prototype, made entirely of aluminum, is produced monolithically using electric discharge machining (EDM). The design incorporates four torsion-reinforced folded leaf springs, effectively reducing parasitic motion and enhancing support stiffness. To meet the specified requirements, a design optimization process is undertaken, carefully considering constraints to attain an optimal CORS configuration. Integration of the CORS with a voice coil actuator for driving force and confocal chromatic sensors for detecting parasitic motion is carried out. Experimental results demonstrate and validate the performance of the CORS.

Keywords: Ultra-linear stage, Compliant mechanism, Sarrus mechanism, Parasitic motions, Monolithic

1. Introduction

Ultra precision mechanisms with one, two, and/or three degrees of freedom (DoF) are the foundation for applications like semiconductor fabrication (Choi et al., 2001; Lee et al., 2006), scanning systems (Kim et al., 2007; Park and Moon, 2005), medical imaging (Van der Maas et al., 2016), and fabrication of nano-devices (Brouwer et al., 2010; Gorman et al., 2006). These industries demand devices that allow for precision motion guidance with a resolution and accuracy in the order of micrometers or even nanometers. For example, in the semiconductor industry it is the trend to make the microchips smaller and faster, with a resolution up to 10 nm (Van Schoot, 2023).

The photonics manufacturing industry is one of those ever more demanding industries as well. The application there can be found in mask and substrate handling. Solak et al. (2011) proposed a promising nanofabrication method that uses the Talbot effect for creating precise nanostructures, particularly suited for photonics applications, called Displacement Talbot Lithography (DTL). The prinicple of DTL requires a varying gap between the mask and substrate. This study focuses on moving the mask, a strategy which holds potential for enhancing coupling dynamics. However, implementing a moving mask is related to a complex building volume. Conventionally, the mask occupies an intermediary position between metrology and a substrate, resulting in a planar volume with restricted height in the direction of motion. Typically, ultra-precision stages integrate a compliant mechanism to facilitate motion guidance.

Compliant mechanisms (CM) use elastic deformation of flexible components to enable a desired motion due to a force or input motion. There are multiple advantages of CM which are preferable for precise positioning. Due to their elastic nature, these mechanisms have no friction, no backlash, and are linearly predictable for small motions (Smith, 2003). Furthermore, CM benefit from the fact that there are no overlapping pieces which can allow a single piece production (Gallego and Herder, 2009). This has a potential for significantly lower costs, due to less assembly and manufacturing time. However, CM are more challenging to design due to their inherent coupling between kinetics and kinematics (Radaelli and Herder, 2016).

CM can be classified into spatial and planar geometries. Spatial geometries includes geometries in the 3D-coordinate system (Howell, 2013). The flexible elements are not in-plane with the motion. Contrary to spatial geometries, planar geometries consist of flexible elements that are in-plane with the motion. Focusing on straight-line mechanisms that are suitable as an ultra-precision stage, the available literature is scarce. Nevertheless, several researchers have developed different types of ultra-linear stages using CM.

Koster (1994) has developed ARCADE. This spatial mechanism is based on a 13-hinge mechanism. The mechanism consists of three monolithic planar mechanisms, symmetrically placed around 120 degrees, which together create a large spatial design of 200x200x200 mm. Along a stroke of 5 mm, ARCADE deviates along axes X and Y with 15 nm and rotates around these axes with 5 μrad. Cosandier (2013) created a 13-hinge based translational stage for the watt balance with a 40 mm stroke. The mechanism deviates 180 nm and 40 nm along the axes X and Y, respectively, while rotations did not exceed 5.3 μrad around the Y axis, and 3 μrad around the X axis. Furthermore, he designed an assembled Sarrus guide, with dimensions 290x290x150 mm. Translational deviations along the X and Y-axis are 200 nm and 500 nm, respectively, while the rotations around X and Y did not exceed 275 μrad and 220 μrad, respectively.

The planar mechanism of Jones (1951) consists of four pairs of leaf springs. These pairs create a mechanism resembling on a symmetric single parallelogram. Along a 10 mm stroke, it deviates with 2000 nm and 500 nm in X and Y direction. The measured parasitic rotations were 10 μrad, 63 μrad, and 136 μrad

around X, Y, and Z-axis, respectively. Furthermore, a linear in-plane motion up to 200 μm was allowed by the translation stage of Becker et al. (1987). The design is a symmetrical and monolithic double parallelogram consisting of circular notches. They claim a smooth translation within one hundredth of a nanometer, and tilts below 1 nrad over the full range of motion. In order to reduce the parasitic motions, they added additional torques proportional to the displacement using magnets.

Planar CM are often used as motion guides in ultra-precision stages (Howell, 2013). These mechanisms are easier to manufacture, resulting in lower cost and improved manufacuring tolerances. However, their motion is in-plane of the flexure, which often results in a large building volume in the direction of motion. Spatial CM, such as the Sarrus mechanism, are often large in size and more difficult to manufacture. However, the Sarrus mechanism is a spatial mechanism that has potential to have a small building volume in the direction of motion. Thus, there is a need of an easy to manufacture Sarrus mechanism with a small building volume in the direction of motion.

In this study, a promising design of a compact ultra-linear Compliant torsion Reinforced Sarrus mechanism (CORS), capable of ultra-linear motion, is presented. Due to its compactness, a less obstructive build volume is needed compared to existing stages. A mathematical model is developed and stiffness values are calculated. A finite element model (FEM) is developed to optimize the CORS with Simcenter HEEDS. Experiments, to verify the FEM model, were conducted on an aluminum 5083-O prototype made by means of electric discharge machining, EDM, whereby the desired shape is obtained by using electrical discharges.

This paper is organized as follows: Section 2 describes the methods used in this study, outlining the design criteria, conceptual design, dimensional design, and the design optimization. In Section 3, the experimental validation is presented, providing detailed descriptions of the test setup, experiments conducted, and the corresponding results. Following this, Section 4 offers a comprehensive discussion on the findings, contextualizing them, and exploring their implications. Finally, Section 5 concludes this paper by summarizing the key findings, reflecting on the significance of the research, and suggesting recommendations for future research.

2. Methods

2.1. Design criteria

In the design of the CORS, design criteria were considered based on the field of application. The reference frame used is where X and Y are situated in the horizontal plane with Z pointing upwards.

The first criterion states that the CORS must enable a platform to perform a 5 mm translation along the Z-axis.

The second criterion states that that the CORS must effectively mitigate parasitic motions of the platform. These motions encompass translations along both the X and Y axes, as well as rotations around the X-axis (Rx, tip), Y-axis (Ry, tilt), and Z-axis (Rz). The cumulative parasitic motion, or total error budget, denoted as e, remains within 5 nm over the final 0.1 mm stroke.

The third criterion involves the stiffness of the CORS. The first eigenfrequency must be below 20 Hz, to limit the actuation force since high forces can lead to high unwanted internal stresses. Furthermore, the second eigenfrequency must be maximized to enhance the controllability, robustness, and dynamic performance.

The last criterion describes the available volume: the CORS has to fit in a rectangular space of 300x300x45 mm. An overview of the design criteria is given in Table 1.

2.2. Conceptual design

The design of the CORS includes a base, flexure mechanism, and platform. These subsystems are responsible for adjusting the platform's position along the Z-axis.

The CORS enables to adjust the platform's position, based on a conventional Sarrus Linkage. The linkage is attached in between the base and the platform. The Sarrus mechanism is a well-know rigid-link mechanism, but relatively unknown as a CM. The linkage, comprising four equal length links organized into two perpendicular groups, is characterized by its utilization of two parallel horizontal plates, the base and platform, arranged vertically, one above the other (Fig. 1). Each group features pairs of hinged bars or plates connecting the horizontal plates, facilitating vertical motion of the upper plate towards and away from the lower one. The hinges enforce constraints, ensuring the connected bars or plates remain in the same plane and maintain axial translation. Mobility analysis indicates a DoF of 0 for the 2-sided Sarrus linkage; however, due to over constraints, the upper platform exhibits vertical mobility. More pairs of hinged bars or plates can be added, increasing the number of over constraints.

The rigid-link mechanism can be transformed to a CM. The plates are replaced with leaf springs, creating two folded leaf springs, oriented 90 degrees from each other, all orientations are possible as long as they are not opposite to each other. In general, the parameters that define the mechanism are the number of flexures, the inter-flexure angle, and the angle between the folded leaf springs. The characteristics defining a single leaf spring are length, width, and thickness.

A folded leaf spring only constrains one DoF, a translation along its folding axis (X-axis in Figure 2). Since it is a spatial mechanism, the torsional compliance of a single leaf spring needs to be taken into account besides the compliance along the

Criterion	Value
DoFs	1 (Z-translation)
Range of motion	5 mm
Cumulative error	5 nm
f_0	$<$ 20 Hz
Volume	300x300x45 mm

Table 1: Overview of the design criteria

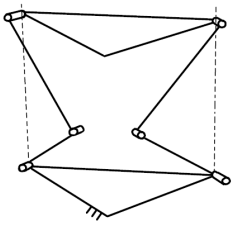

Figure 1: Schematic Sarrus Linkage

X, Y, and Z-axis. The torsional stiffness is:

$$K_t = \frac{GJ}{L} \tag{1}$$

where $J = \frac{1}{3}dt^3$ is the torsion constant and G the shear modulus. Increasing this torsional stiffness results in constraining one more DoF. The bending stiffness around the folding axis, X, is:

$$K_{rx} = \frac{EI_{rx}}{L} \tag{2}$$

where the area moment of inertia around the folding axis is $I_{rx} = \frac{1}{12}dt^3$.

Furthermore, the in-plane bending stiffness has to constrain an additional DoF. The in-plane bending stiffness of the leaf spring is:

$$K_{ipb} = \frac{EI_{ipb}}{L} \tag{3}$$

where $I_{ipb} = \frac{1}{12}td^3$. This has a higher order of magnitude relative to the K_t and K_{rx}. Therefore, it is assumed as constrained. A torsion reinforced folded leaf spring will results in constraining three DoF.

Increasing torsional stiffness is achieved by incorporating torsion reinforcement structures onto the leaf springs. These structures, previously introduced by Rommers et al. (2022), are used to create a flexure joint with high stiffness in its support directions or function as rotational constraints for a folded leaf spring. The structures behave like leaf springs resulting in a smooth strain distribution, contrasting with rigid-links that induce peaks in the distribution. As a results, two new parameters are introduced: n and γ, where n is the number of reinforcements (further referred to as teeth) and γ is the angle of the teeth leaf springs relative to the original leaf spring.

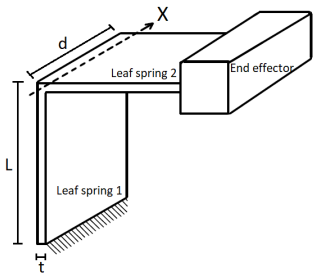

Figure 2: Illustration of single folded leaf spring and end effector

By adding an extra folded leaf spring, in this case oriented at 90 degrees relative to the first folded leaf springs, three constraints are added. Resulting in one overconstraint, which is the in-plane bending of the folded leaf springs. The DoF is a translational motion perpendicular to both folding axes.

There is chosen for four folded leaf springs with torsion reinforcements due to manufacturability and symmetry, which also results in a centered center of stiffness which is proven to be beneficial to minimize parasitic motions (Meinders, 2021). The width of the flexures have influence on the reliability of the EDM manufacturing process. The effective spark height must be minimized to reduce manufacture errors. The configuration with four folded leaf springs leads to a minimized spark height while maintaining high support stiffness. Due to a centered centre of stiffness, it is easier to actuate in the center of stiffness because it is precisely known, which is another strategy to prevent parasitic motion according to Meinders. This configuration (Fig. 3) results in an overconstrained system, which can result in unwanted stresses. However, adding overconstraints has been proven beneficial in some cases and have less influence in a monolitic structure.

Thought experiments can provide valuable insights into the influence of parameters on the desired performance of the CORS. Each parameter within the CORS must be carefully defined based on trade-offs. For example, the thickness and width of flexures should ideally be maximized to enhance constraint levels. However, this maximization is constrained by the need to maintain a low eigenfrequency. Additionally, minimizing the inter-flexure angle is advantageous for reducing the stiffness in the direction of motion and increasing lateral stiffness, while an angle of zero theoretically leads to a mechanism reliant on leaf spring compression. However, this angle is limit due to manufacturability.

Another parameter to consider is the number of teeth, which involves a trade-off between building volume and torsional stiffness. Increasing the number of teeth reduces building volume, assuming a constant γ, while enhancing torsional stiffness. However, this also leads to increased stiffness in the direction of motion, potentially requiring multiple triangles to bend in a chain-like manner. Achieving an optimal balance among these parameters is essential for designing the CORS that meets performance requirements while minimizing constraints.

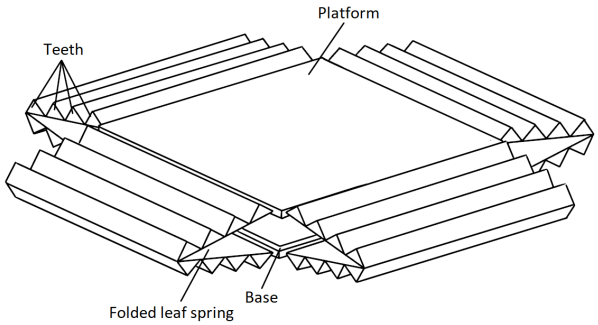

Figure 3: Illustration of conceptual design

2.3. Dimensional design and modelling

2.3.1. Design parameters and performance metrics

The flexures of the mechanism can be defined by the parameters illustrated in Figure 4. The thickness of the top and bottom flexure is defined as t_t and t_b, respectively. Furthermore, the width of the platform and flexure are defined as b and d, respectively. The number of so-called teeth is addressed with n_t and n_b.

The performance metrics are position and travel accuracy, the first and second eigenfrequency, and height in drive direction.

2.3.2. Stiffness analysis

Direct method is used for a numerical 3D beam finite element analysis considering bending, small displacements and no cross-axis couplings.

$$\mathbf{f} = \mathbf{K}\mathbf{d} \tag{4}$$

with **f** as the nodal load vector with three forces along and three moments around the XYZ-axes for each node, **K** the system matrix, and **d** as the nodal displacement vector with three translations along and three rotations around the XYZ-axes for each node, all in the local coordinate system.

The local elements stiffness matrix has to be transformed to the global coordinate system. The transformation is performed by the transformation matrix, **T**, and can be expressed as:

$$\mathbf{K}_{global} = \mathbf{T}^T \, \mathbf{K}_{local} \, \mathbf{T} \tag{5}$$

Once all local element stiffness matrices are computed, the system matrix, **K**, can be assembled. The assembling is done by adding up the virtual work belonging to each of the elements, resulting in the mathematical equivalent of putting the mechanism together:

$$\mathbf{K} = \sum K_{global,1} + \cdots + K_{global,n} \tag{6}$$

The material used for EDM fabrication of the prototype is aluminum, Al 5083-O. The values of $\alpha, \beta, \gamma_1{=}\gamma_2, L_1{=}L_2, t_1{=}t_2, n_t{=}\, n_b$, and $b{=}d$ of the flexures are 5 deg, 10 deg, 75 mm, 0.6 mm, 1, and 80 mm. The numerical approached value of f_0 is 30 Hz and f_1 is 222.4 Hz, assuming a mass of 700 grams.

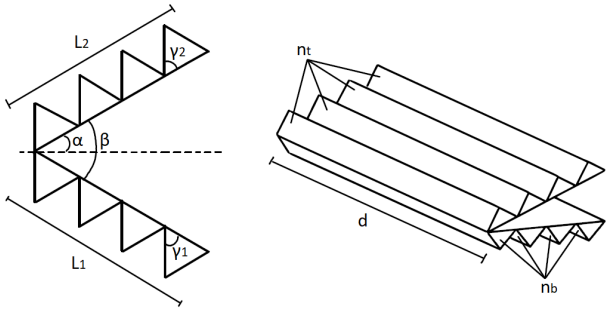

Figure 4: Illustration of flexure parameters

2.3.3. Optimization in Simcenter HEEDS

To find the optimal design of the CORS, Simcenter Heeds of Siemens (HEEDS) is used. HEEDS can help to gain an insight into the design space, and could find an optimal design according to multiple design criteria and constraints. HEEDS is combined with other packages, for instance, of Siemens: NX and Simcenter. NX is used to define a conceptual sketch. Thereafter, a mesh and simulation is generated with Simcenter. These are used by HEEDS to optimize and explore the design and design space.

HEEDS contains a search strategy called SHERPA. SHERPA employs a multi-faceted approach during a single search, utilizing multiple search methods. The selection and how it uses these multiple search methods is commercially unknown. This strategy leverages the strengths of each method while dynamically diminishing the involvement of ineffective methods throughout the search process (Siemens, 2008). HEEDS gives each design a performance rating. The value returned for the objectives and the degree to which a design satisfies its constraints determine the design's performance function. A high-performance design is one that satisfies all constraints and has a good rating on its objectives. In this study, it is considered that an optimal design is found when the performance has not improved after 200 additional designs. A typical HEEDS iteration includes: 1) Create sketch based on design parameters; 2) Create new mesh; 3) Run simulation; 4) Post-Process output; 5) Generate new design parameters. This process stops until a defined amount of designs is generated and computed. Furthermore, HEEDS shows the influence of each parameter on the performance criteria, which helps to gain insight into the design space.

Design parameters

To ensure flexural symmetry, design parameters are dependent on each other:

$$\begin{aligned} 2\alpha &= \beta \\ L_1 &= L_2 = L \\ t_1 &= t_2 = t \\ \gamma_1 &= \gamma_2 = \gamma \\ n_t &= n_b = n \end{aligned}$$

Resulting in the design vector:

$$\mathbf{x} = \begin{bmatrix} \alpha & L & t & \gamma & d & b & n \end{bmatrix}$$

The bounds of **x** are given in Table 2. The bounds are dependent on the specified volume claim and considerations of manufacturability. The lower boundaries for the thickness, t, and the inter-flexure angle, represented by 2α, are related to the limitations of EDM, as informed by the manufacturer's knowledge and assurance. Furthermore, the selection of aluminum 5083-O as the material of choice accelerates the EDM process by a factor of three in comparison to stainless steel or titanium, resulting in reduced costs. Furthermore, the 5083 alloy is cast, resulting in low to zero internal stresses inside the initial workpiece. Minimal internal stresses is preferred to

Variable	Lower Bound	Upper Bound
α	5	90
L	10	150
t	0.6	1
γ	5	89
d	10	250
b	152	250
n	0	6

Table 2: Design parameters and their bounds

Parameter	Optimized Value
α, β	5 deg
L	75 mm
t	0.6 mm
γ	27 deg
d	80 mm
b	152 mm
n	1

Table 3: Optimized values design parameters

prevent geometrical imperfactions when the flexures gain their compliance.

Mesh

The mesh should be converged for every design HEEDS generates. Therefore, the mesh should be controlled to ensure a converged robust mesh. In this case, the 2D mesh is used to create an easier controlable surface compared to a 3D solid. The commonly used requirement to use shell elements is that the length characteristic must be way larger than another parameter: L>>t, in this case. The benefit of using shell elements is the reduction of computation time relative to solid elements, while maintaining accuracy. This is beneficial for HEEDS while the computation time will be much shorter, and still an insight is obtained into the design space.

Simulation in Simcenter 3D

The optimization criteria are computed using the simulation software within Simcenter, NASTRAN. One end of the flexures is constrained in all DOF using a user defined boundary condition. The enforced displacement acts in the center of the platform. Two solutions contribute to computing the optimization criteria, a modal analysis (SOL 103) and a multi-step non-linear analysis (SOL 401). The outputs are the parasitic translations in the center of the platform, and the first and second eigenmode of the CORS.

Optimization problem

The optimization problem can be formulated. The goal is to maximize the difference between the first eigenmode, vertical translation of the platform, and second parasitic eigenmode. This should be obtained while maintaining stiffness, error, mechanical stress, volume, and manufacturability constraints. Most algorithms benefit from a minimization problem therefore it is rewritten into a negative null form:

Minimize

$$\frac{f_0}{f_1}$$

Subject to

$$\begin{aligned} f_0 - 20 &\leq 0 \\ e - 5 \times 10^{-9} &\leq 0 \\ \sigma_y - 150 \times 10^6 &\leq 0 \\ Z_{vol} - 45 \times 10^{-3} &\leq 0 \end{aligned}$$

and

$$\underline{\mathbf{x}} \leq \mathbf{x} \leq \bar{\mathbf{x}}$$

Optimization results

The optimal design can be seen in Figure 5, and each individual parameter is shown in Table 3. In the optimization, $\alpha = 5\,\text{deg}$, $b = 152mm$, and $t = 0.6mm$ reached there lower bound. More optimal design can be found when these bounds are relaxed. However, these bounds are related due to manufacturing. Furthermore, the optimal design reached the eigenfrequency constraint of 20 Hz and the height constraint of 45 mm. All angles are replaced by fillets to ensure manufacturability and no peak stresses.

The FEA of the design can be seen in Figure 6. The maximum stress is 0.9 MPa for a 103 μm stroke due to a 1.5 N force. Notice that the flexures bend as a whole, which leads to lower stress peaks.

Furthermore, in Table 4 the results of the numerical, shell, and solid model are given.

3. Experimental validation

3.1. Test setup

A measurement setup has been designed with the capability to accurately measure in six DoF, achieving a resolution of 5 nanometers. This setup consists of an aluminum framework and

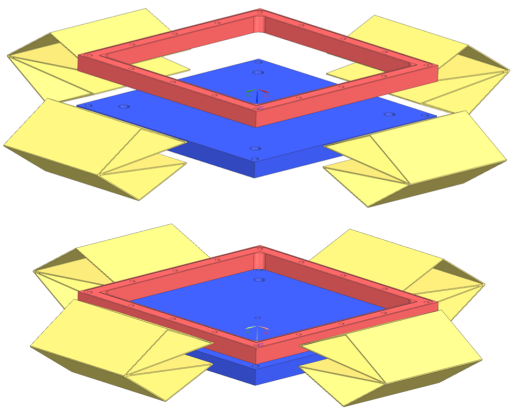

Figure 5: Dimensional CAD model of the CORS including flexure base, flexure mechanism, and platform

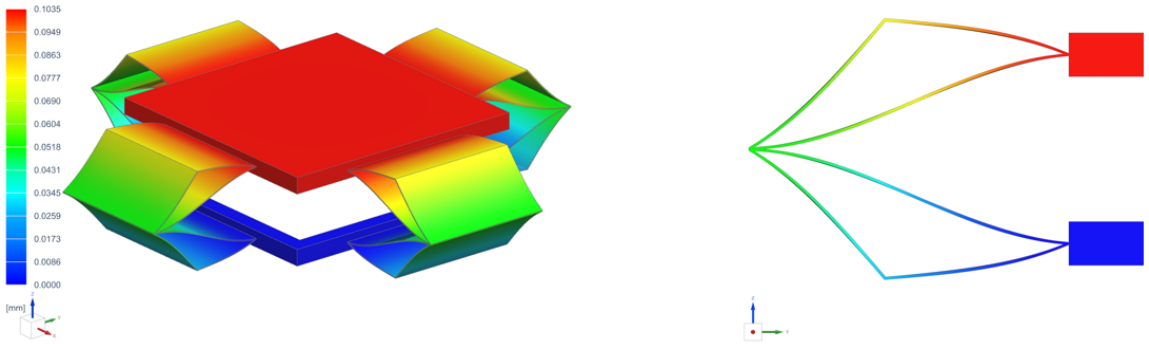

Figure 6: Left: FEA overview CORS. Right: FEA cross-section of torsion reinforced flexure

	Numerical	Shell Model	Solid Model
f_0 [Hz]	30.7	21.2	22.4
f_1 [Hz]	222.4	173.2	177.4
Error$_{f_0}$ [%]	27%	5.6%	-
Error$_{f_1}$ [%]	20.2%	2.3%	-
Error (x;y) [nm]	-	1.24E-5	2.52E-1

Table 4: Simulated stiffness and error with the solid model as reference

base plate, 3D-printed interfaces for all sensors and the actuator, and the CORS itself (see Figure 7). Positioned atop rubber adjustable feet upon a vibration isolation table of TMC from 3 Hz with minimal amplification of resonance (8-12dB).

3.1.1. Drive system

The CORS is actuated using a voice coil actuator (Akribis AVM40-HF-6.5) and a 3D-printed parallelogram based linear guide connected by a thin copper wire, to decouple the CORS and actuator. Voice coil actuators are direct drive actuators known for their precise linear motion with low hysteresis. A smooth repeatable motion is preferred to obtain low noise measurements. A function generator (Tektronix AFG1062), with a maximum output current of 0.1A, will be the input signal, while the actuator needs a current of 0.29±0.095A. To generate a 6±2N force, a voltage follower is needed. This is realized using a power OPAMP (LM3886T) in a non-inverting circuit combined with a voltage divider. The typical circuit, with gain 1, is simulated in PSpice beforehand.

3.1.2. Sensors

The optical sensors are based on the chromatic confocal distance measurement principle (Ruprecht et al., 2005). It consists of a control unit, ©*Precitec Optronik GmbH CHRocodile 2 DPS*, optical fibers, and optical probes with a 1.2 mm measuring range. Each control unit is suitable for two probes. The prototype will be measured with four sensors, therefore two control units are needed. The probes are perpendicular mounted, through 3D-printed interfaces, facing $\lambda/20$ rectangular mirrors.

3.1.3. Test plan and preconditions

First, a 3D-scan is made of the prototype, to check the exact dimensions. This is done with the ZEISS T-SCAN hawk 2,

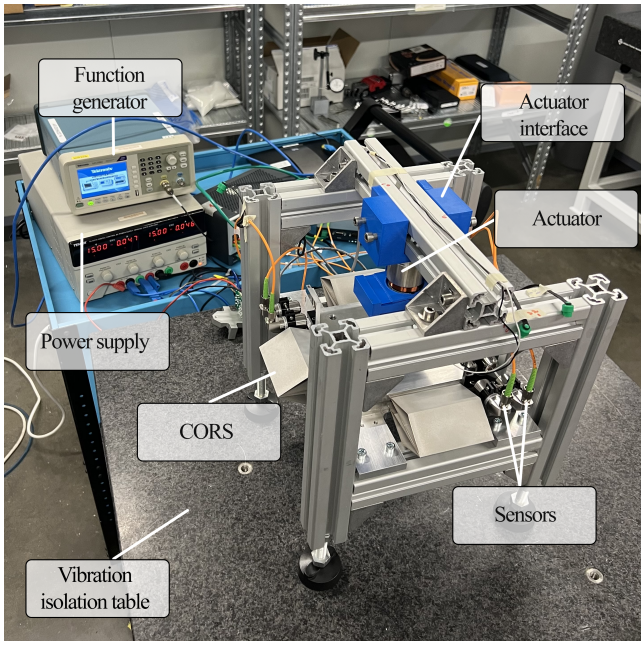

Figure 7: Test setup

which results in a scan that can be compared with the CAD-model to gain an insight into manufacture imperfections.

The sensors and actuator have to be calibrated. The sensors have to be halfway their 1.2 mm measuring range, and the needed input voltage has to be found for at least 100 μm stroke.

The eigenfrequencies can be measured with the sensors themselves. The CORS is triggered, and a fast Fourier transform (FFT) can be obtained from the triggered motion, resulting in the estimated eigenfrequencies.

To measure the parasitic motions in six DoF, the sensors are relocated once, since there were four sensors available. First, three sensors measured the tip and tilt motions along a Z-stroke of 140 μm. Thereafter, the sensors were replaced and the X and Y translation were measured along a 140 μm Z-stroke together with the rotation around the Z-axis. The measured distances are transformed to translations taking the average, and the rotations by dividing the difference between distances and the location relative to each other.

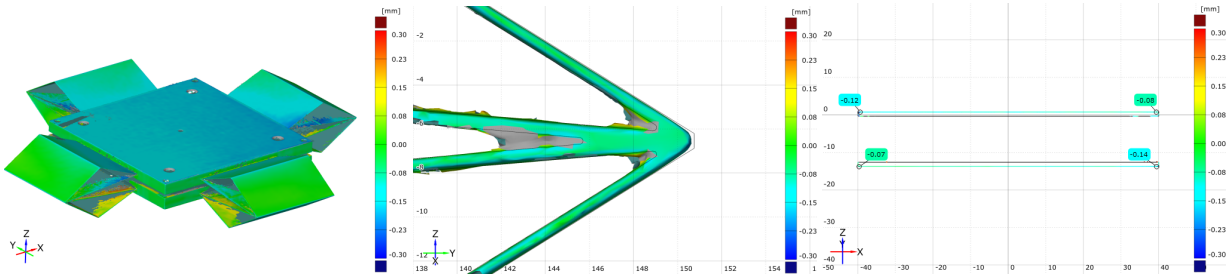

(a) CORS overview (b) Fillet R=0.15 (c) Flexure alignment

Figure 8: 3D scan

3.2. Results

3.2.1. 3D-scan

Visual inspection revealed no big manufacture defects. Most of the flexure has uniform thickness along the length and width of the flexure. Visually noticeable defects are a small bump in the middle of the inner flexures and not constant radius for all the fillets. The 3D-scan confirmed these findings and it can be seen in Figure 8.

3.2.2. Stiffness measurement

The measured horizontal and vertical stiffness estimated through a FFT can be found in Figure 9. The first eigenfrequency and its harmonics can be seen at 20.35 Hz and its multiples, respectively. Furthermore, small peaks are observed at approximately 187 Hz suggesting the second, third, and a harmonic of the first eigenfrequency.

3.2.3. Parasitic motions

The parasitic motions along the Z-stroke are plotted in Figure 10. A linear error is shown for the parasitic X and Y translation, 0.838 nm/μm and 0.636 nm/μm, respectively. The tip, Rx, error has a range of approximately 6 μrad along the Z stroke. The tilt, Ry, error has a range of approximately 4 μrad. The measured parasitic rotation around the Z-axis is 1.44 nrad/μm stroke.

Furthermore, a repeatability and hysteresis of approximately 10 nm and 15 nm is achieved, respectively.

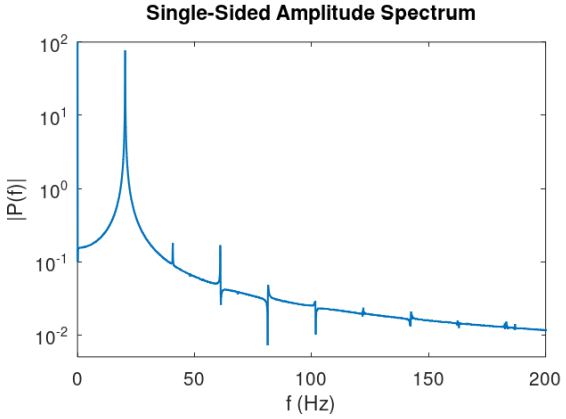

Figure 9: Measured FFT where f_0 = 20.35 Hz and $f_{1,2} \approx$ 185 Hz

4. Discussion

This design of a compact ultra-linear compliant torsion reinforced Sarrus mechanism resulted in a smaller design compared to the existing literature. The CORS occupies a less obstructive building volume of approximately 300x300x45 mm.

The optimized CORS has a inter-flexure angle $2\alpha = 10$ deg, corresponding to the lower bound. This is expected while a small angle results in a higher support stiffness and low stiffness in the direction of motion. In theory, this angle could be made very small but still nonzero. If the angle is zero, it is analogue to a single leaf spring with a shortening effect during motion. However, the minimal radii of the fillets limited by the manufacturing process constrain the angles.

Furthermore, the thickness of the flexures, $t = 0.6mm$, also reached their lower bound. Reducing the thickness will result in lowering the stiffness in drive direction in the order of power 3, while other stiffnesses reduce linearly. The thickness could theoretically be reduced to find better design. However, practical constraints within manufacturing processes result in unfeasible design. Consequently, a minimum threshold of 0.6 mm was prescribed for this parameter.

An advantage is that the CORS is created monolithically. The CORS has multiple overconstraints in rotation and translation around and along all axes. This could lead to asymmetric stresses due to potential temperature gradients, for instance. However, this effect is minimized due to its monolithic structure.

The performance of the CORS is characterized by the travel and position accuracy and the first and second eigenfrequency. The translational error along the X and Y axis are 0.838 nm/μm and 0.636 nm/μm, respectively. However, these errors are including misalignment of the mirrors relative to the direction of motion and the sensors, which will artificially affect the travel accuracy due to an Abbe error. Furthermore, the sensors have a certain drift over time due to change in external conditions. These errors are linear, therefore they can be filtered resulting in Figure 11. The corrected error along the X and Y axis are now within 10 nm for a 140 μm stroke, respectively. The measurements are now limited to the resolution of the sensors, mostly noise is observed. A fitting suggests no error along the X and Y axis, respectively.

The measured rotation around Z revealed a rotation of 1.44 nrad/μm. This results in a translational error on each platform's

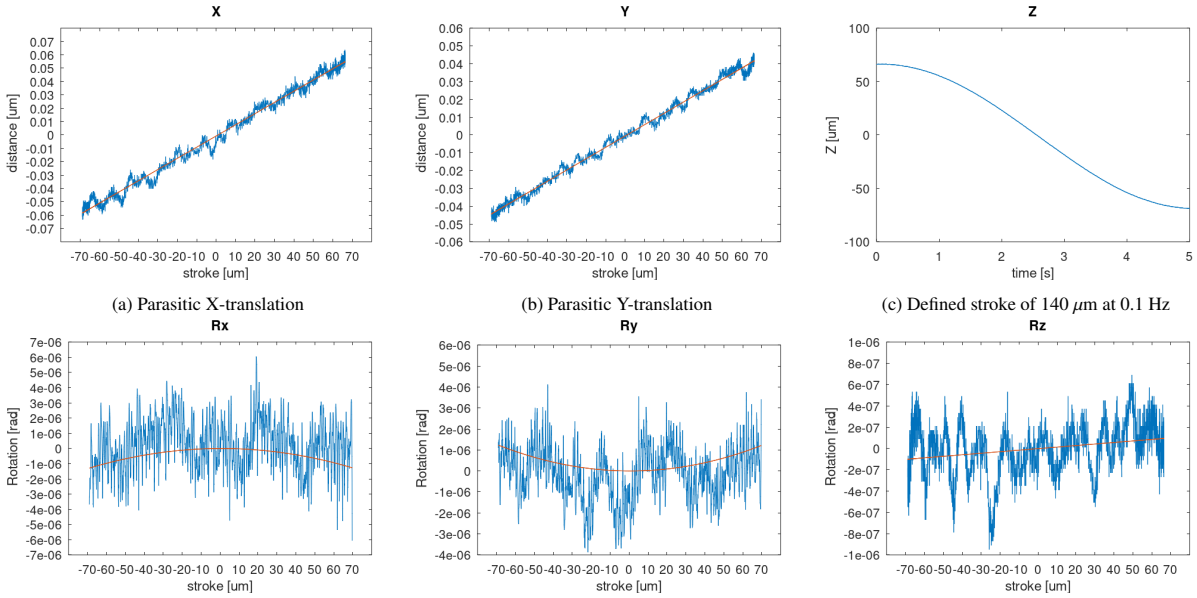

(a) Parasitic X-translation (b) Parasitic Y-translation (c) Defined stroke of 140 μm at 0.1 Hz

(d) Parasitic X-rotation (e) Parasitic Y-rotation (f) Parasitic Z-rotation

Figure 10: Parasitic motions over 140 μm stroke

corner of approximately 14 nm. The measured tip and tilt errors, Rx and Ry, have a range of approximately 6 μrad and 4 μrad over the Z stroke.

The errors could be the results of the flatness of the mirror and the actuator alignment. The flatness deviation of the mirror is $\lambda/20$ corresponing to 0.025 μm for visible light ($\approx$500 nm). The deviation will cause the reflected light to be slightly distorted from its ideal position. Considering a flat mirror, we can assume that the radius of curvature is effectively infinite. Therefore, the lateral displacement is equal to the flatness deviation, 25 nm.

FEM revealed that the actuator alignment has influence on the travel accuracy. It showed that if the load vector has an angle with the X and Y axis of 5.7deg instead of 90deg that the position accuracy is 22 nm in both X and Y direction.

This is also an opportunity, the measured linear error can also be calibrated physically. Figure 12 shows the translational error over a 140 μm stroke due to the angled actuator force, resulting in a normal and shear force. The measured translational X is 0.024 nm/μm. This suggests that the CORS can be calibrated even if the CORS itself does not enable a perfectly linear motion.

Mass upon the platform has been added to correct for the tip and tilt error. It had no influence, this suggests a stiff CORS in Rx and Ry. However, more research is needed to obtain more precise information of the parasitic motions around X and Y axis.

Figure 8 shows the 3D-scan of the CORS manufactured through EDM. Visual inspection revealed manufacturing errors, which are confirmed by the scan. Such as, non-uniform radii in the fillets of the flexure. All fillets are of different size and radii, for instance the fillets seen in Figure 8b. This could lead to asymmetric flexures with different effective length. However, the advantage of the design is that imperfections have less influence on the motion path while the flexure constrain motion in all directions except a Z-translation. Furthermore, a small bump in the middle of the flexures is seen as a result of the start of the EDM process. Nevertheless, it did not affect the func-

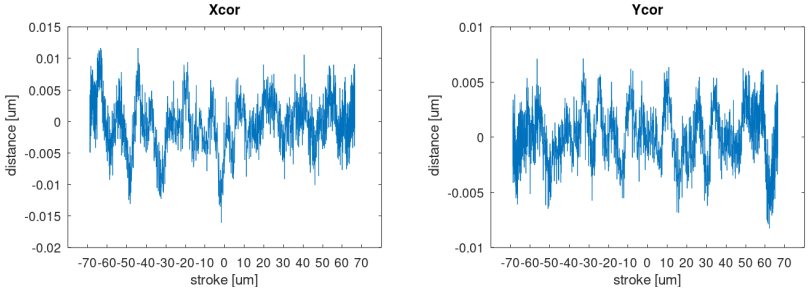

(a) Corrected parasitic X-translation (b) Corrected parasitic Y-translation

Figure 11: Corrected parasitic X- and Y-translation

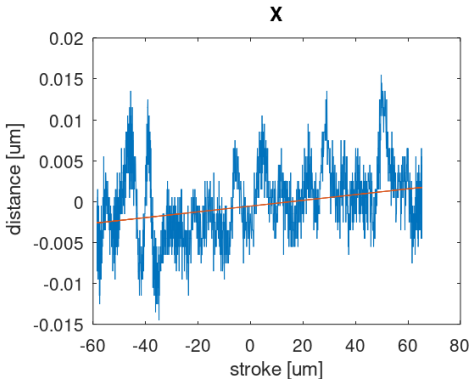

Figure 12: Parasitic X-translation after X-calibration

tionality of the CORS, it can be concluded that errors close to the fillets and the bump of in the middle are functionally acceptable. However, to prevent these errors changes can be made in the design and manufacture process.

The alignment of the flexure can be seen in Figure 8c. The flexures should be perfectly aligned in the horizontal plane to prevent parasitic error. However, a deviation of at least 4 μm is measured suggesting that the flexures are not aligned perfectly, corresponding to a misalignment of 0.5 mrad to the horizontal plane. The influence of this misalignment has been investigated using the FEM. The misalignment around the Y-axis of the two opposite flexure resulted in a translational error of 69 nm in X. In practice, there is an exceedance of the total error budget of 5 nm. Therefore, more research has to be done in the manufacturing strategy. The alignment must be done carefully to mitigate these errors.

The FFT in Figure 9 shows an eigenfrequency of 20.35 Hz and approximately 185 Hz. Comparing to the simulation the errors are within 10% and 5.4%, respectively. The magnitude of the parasitic eigenmode, f_1, is roughly 10^4 times smaller than of the first eigenmode f_0. To increase the magnitude and accuracy of f_1, a different measuring method can be used. For instance, with accelerometers and a known trigger, like an impact modal hammer. Furthermore, the difference could be explained by a deviation in mass, Young's modulus, and stiffness introduced by manufacturing imperfections. The most critical modes are the first X and Y modes and the rotational mode around Z having direct effect on the parasitic errors. These are not measured and should be investigated in the future.

The measured repeatability and hysteresis could be the results of friction and/or an error due to temperature drift. There are a few spots were friction can occur. First, the copper wire is stretched between two ring bolts. Tension within the wire could lead to slip between the bolt and wire. Furthermore, within the actuator friction can occur when the moving coil is not perfectly aligned to the permanent magnet.

To gain insight into the manufacturing tolerances, a small tolerance analysis has been done. The parameter with most influence is the thickness of the flexure. The manufacturing tolerance on the thickness is 0.02 mm. The applied tolerance gave a translational error of 11 nm. A more extensive analysis has to been done, to obtain more information about the tolerances which can lead to a more robust design.

The fatigue life of the CORS was out of scope of this study. However, some remarks can be done. The surface roughness was quite rough which impacts the fatigue life negatively. This roughness can be reduced by repeating the EDM process multiple times. Furthermore, a postprocessing can be used to reduce the surface roughness, for instance glass bead blasting.

In terms of measuring, changes in environmental conditions influence the accuracy of the chromatic confocal sensors. Changes in atmospheric density alter the index of refraction, affecting the wavelength of light in the sensors. This can introduce errors in distance measurements, compromising accuracy. Calibration and environmental controls can help mitigate this effect.

Furthermore, thermo-mechanical drifts refer to changes in a system's behavior due to temperature fluctuations and mechanical stresses. These drifts can affect the stability and accuracy of measurements in various devices and instruments, including sensors and precision equipment. To minimize their impact, proper thermal management and mechanical stabilization techniques are often employed, such as environmental control.

5. Conclusion

In conclusion, the design of the CORS represents a significant advancement in compact mechanism design, offering a compact monolithic design while maintaining critical performance metrics.

The optimization process has resulted in a mechanism with small measured parasitic motions. The translational errors along the X and Y axis are 0.838 nm/μm and 0.636 nm/μm, respectively. The assumption that the linear errors are the result of drift and Abbe errors, resulted in errors below 10 nm for both translations. The rotational errors over a 140 μm stroke are within 6 μrad and 4 μrad around the X and Y-axis. Furthermore, a small rotation occurs around the Z-axis of 1.44 μrad/μm.

The CORS has its first desired eigenfrequency at 20.35 Hz and the first parasitic eigenfrequencies around 185 Hz.

Challenges such as manufacturing imperfections and misalignments were identified, highlighting the need for meticulous manufacturing processes and alignment procedures. Additionally, considerations for environmental effects on measurement accuracy, such as changes in atmospheric conditions and thermo-mechanical drifts, underscore the importance of calibration and environmental controls in ensuring reliable performance. Future research directions include further analysis of manufacturing tolerances, more complex measurement setup, exploration of modal characteristics, and considerations for improving fatigue life through surface treatment techniques.

In general, this study provides valuable insights into the design and optimization of a compact ultra-linear compliant torsion reinforced Sarrus mechanism, with promising results for high-accuracy motion control systems.

References

Becker, P., Seyfried, P., Siegert, H., 1987. Translation stage for a scanning x-ray optical interferometer. Review of scientific instruments 58, 207–211.

Brouwer, D.M., De Jong, B., Soemers, H., 2010. Design and modeling of a six dofs mems-based precision manipulator. Precision Engineering 34, 307–319.

Choi, B., Sreenivasan, S., Johnson, S., Colburn, M., Wilson, C., 2001. Design of orientation stages for step and flash imprint lithography. Precision Engineering 25, 192–199.

Cosandier, F., 2013. Conception d'axes motorisés rectilignes d'ultra-haute précision. Technical Report. EPFL.

Gallego, J.A., Herder, J., 2009. Synthesis methods in compliant mechanisms: An overview, in: International Design Engineering Technical Conferences and Computers and Information in Engineering Conference, pp. 193–214.

Gorman, J.J., Kim, Y.S., Dagalakis, N.G., 2006. Control of mems nanopositioners with nano-scale resolution, in: ASME International Mechanical Engineering Congress and Exposition, pp. 151–159.

Howell, L.L., 2013. Compliant mechanisms, in: 21st century kinematics: The 2012 NSF Workshop, Springer. pp. 189–216.

Jones, R., 1951. Parallel and rectilinear spring movements. Journal of Scientific Instruments 28, 38.

Kim, D., Lee, D.Y., Gweon, D.G., 2007. A new nano-accuracy afm system for minimizing abbe errors and the evaluation of its measuring uncertainty. Ultramicroscopy 107, 322–328.

Koster, M.P., 1994. Constructies voor het nauwkeurig bewegen en positioneren. Mikroniek 34, 38–42. doi:https://www.dspe.nl/wp-content/uploads/1994/02/Mikroniek-Issue-2-1994.pdf.

Lee, J., Choi, K.B., Kim, G.H., 2006. Design and analysis of the single-step nanoimprinting lithography equipment for sub-100 nm linewidth. Current Applied Physics 6, 1007–1011.

Van der Maas, R., van der Maas, A., Dries, J., de Jager, B., 2016. Efficient nonparametric identification for high-precision motion systems: A practical comparison based on a medical x-ray system. Control Engineering Practice 56, 75–85.

Meinders, N., 2021. Compensating parasitic motions and cross-couplings in compliant mechanisms: The development of a new compensation strategy to diminish unwanted motions .

Park, J., Moon, W., 2005. An xy scanner with minimized coupling motions for the high speed afm, in: Proceedings of the Korean Society of Precision Engineering Conference, Korean Society for Precision Engineering. pp. 653–656.

Radaelli, G., Herder, J., 2016. A monolithic compliant large-range gravity balancer. Mechanism and Machine Theory 102, 55–67.

Rommers, J., Naves, M., Brouwer, D., Herder, J.L., 2022. A flexure-based linear guide with torsion reinforcement structures. Journal of Mechanisms and Robotics 14, 031013.

Ruprecht, A.K., Pruss, C., Tiziani, H.J., Osten, W., Lucke, P., Last, A., Mohr, J., Lehmann, P., 2005. Confocal micro-optical distance sensor: principle and design, in: Optical Measurement Systems for Industrial Inspection IV, SPIE. pp. 128–135.

Siemens, 2008. SHERPA – An Efficient and Robust Optimization/Search Algorithm. Technical Report WP-1023. red cedar Technology.

Smith, S.T., 2003. Foundations of ultra-precision mechanism design. volume 2. CRC Press.

Solak, H.H., Dais, C., Clube, F., 2011. Displacement talbot lithography: a new method for high-resolution patterning of large areas. Optics express 19, 10686–10691.

Van Schoot, J., 2023. The moore's law machine: The next trick to tinier transistors is high-numerical-aperture euv lithography. IEEE Spectrum 60, 44–48.

A

Displacement Talbot Lithography

The application of the design expounded in this article finds utility in a positioning module integral to a Displacement Talbot Lithography (DTL) apparatus. DTL, an innovative and adaptable nanofabrication technology, capitalizes on the Talbot effect to generate periodic nanostructures.

The Talbot effect, a well-documented phenomenon, manifests when a monochromatic collimated light illuminates a periodic structure, thereby generating self-images of the grating pattern at regular intervals subsequent to the grating (Talbot, 1836). DTL represents a modified iteration of Talbot lithography, boasting a larger Depth of Field (DOF) as a distinctive advantage, thereby rendering it a more robust methodology. This attribute allows for the utilization of non-planar substrates or thick photoresists.

To overcome the DOF problem, DTL employs the strategy of illuminating the mask with a beam possessing a broad spectral bandwidth (Solak and Ekinci, 2005). Through this technique, the diverse wavelength components of the transmitted light field overlap, and beyond a certain distance from the mask, they overlap to form an image that remains invariant with respect to further increases in distance.

Though the initial position of the substrate holds no sway over the final outcome, the stipulated positioning requirements is predicated upon relative positioning. The gap between the mask and substrate must vary for a minimum of one Talbot length, defined as:

The schematic figures below represents the fundamental procedural steps of a DTL process. 1) First, the gap between the mask and substrate must be reduced till the DOF; 2) When the light source is enabled a Talbot field occurs; 3) The mask has to move at least one Talbot Length; 4) The gap between mask and substrate must be increased to make space for a substrate handler.

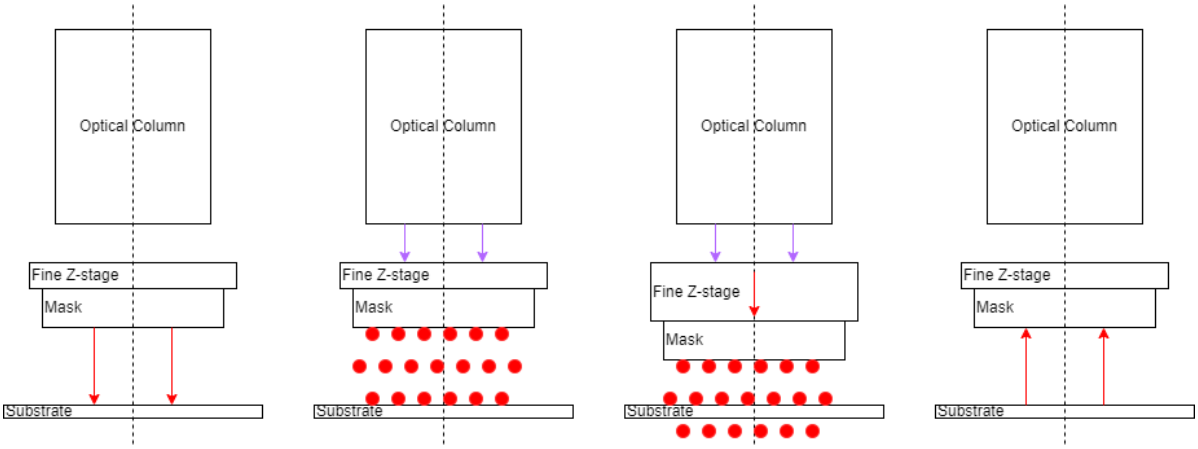

Figure A.1: Typical DTL Process

B

System Overview

[redacted] This module facilitates the adjustment of the gap between the substrate and mask through the movement of the substrate. [redacted] This alteration introduces distinct volume requirements for these assemblies compared to their previous operational configuration.

B.1. Volume Claim

The assertion regarding volume is [redacted] provided by the client. By integrating the module into the schematic topology, a comprehensive understanding of the available volume is attained. To secure the mask onto the mask holder, a vacuum channel with clamping functionality is employed, necessitating an unobstructed surface on the mask. Ensuring unhindered access for the light source to reach the mask necessitates designing around a 6-inch mask. Within a confined volume with a height limitation of 45 mm, dictated by the presence of metrology equipment above the mask.

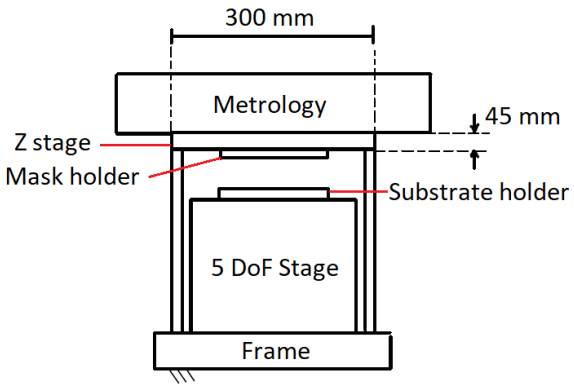

Figure B.1: Volume overview

C

Functional Requirements

The functional requirements are based on the expected volume claim and desired performance, based on talks and brainstorming. They are structured according to Tom Gilbs' method.

	Functional Requirement	Strategy	Specification
1	Bridging a distance in Z-direction between substrate and mask	• Move the mask • Move the substrate • Move mask and substrate • Separate in Rough + Fine Z-stage	[redacted]
2	Maintain high accuracy in centre during 1DOF linear motion	• High stiffness in 5 DOF excluding Z-direction - Compliant Mechanisms - Bearing - Magnetic guiding • Perfectly constrained system • Minimize structural loop	
3	Achieve repeatable positioning between reference plane and POI	• Minimize friction • Minimize hysteresis - No friction • Minimize parasitic vibrations • Control loops • Minimize uncertainties	
4	Adjustable speed actuation in Z-direction	• Continuous - Piezoelectric actuators - Electromagnetic actuators - Linear motors - Electrostatic actuators - Voice-coil actuators • Variable transmission + actuator - Gearing - Lever	
5	System should be integrated	• Design for known interfaces	
6	Minimize internal vibrations	• Minimize mass • Minimize actuators • Counter forces • Minimize moving objects • Static and Dynamic balancing • Actuate CoG • Proper allignment	
7	System should handle different thicknesses of wafers	• High resolution movement • High resolution sensing • High load capacity	
8	Sense displacement between reference plane and POI	• Laser light position sensor • Capacitance sensor • Predicting movement	
9	Design should be inside volume claim	• Build around mask (Coca-Cola can) • Z-stage in positioning stack (rectangular block)	

D

Concepts

D.1. Concept Generation

D.1.1. General Bearings

	Rollerbearing	Airbearing	Flexures	Dry slideways	Ferrofluid bearing
Stroke	Theoretical infinite stroke	Theoretical infinite stroke	Small stroke	Theoretical infinite stroke	Theoretical infinite stroke (fluid dependent)
Travel Accuracy	Based on elastic deformation	Spatial Averaging creates high accuracy	Parasitic motions should be compensated	Based on elastic deformation	Change of film height
	Geometrical and Material Imperfections	Gravity load induces sagging	Predictable errors	Geometrical and material imperfections	Film decreases due fluid trail
	Guidance and roundness quality	Hard to passively control			Stiffness is limited due fluid
Repeatability	Friction	IBSPE provides 300pm	No friction but predictable fatigue	Friction	Based on operating conditions
Stand-still performance	High stiffness	Jitter of 0.32 nm by ISBPE	Actuator dependent	High stiffness	High stiffness when stationary
Load Capacity	Typical High	Moderate	Moderate	High	Moderate
Simplicity	Guiding, sensing, actuator	Guiding, sensing, actuator, pump, controller	Guiding, sensing, actuator	Guiding, sensing, actuator, controller	Guiding, sensing, actuator, pump, controller

Table D.1: Type of bearings

D.1.2. General Actuators

Table D.2: Comparison of Different Types of Actuators

Actuator Type	Piezoelectric	Electromagnetic	Electrostatic	Electrothermal	Electrostrictive
Stroke	Small	Medium to Large	Small	Small to Medium	Small to Medium
Linear Motion	Very High	High	Moderate	Moderate	Moderate
Repeatability	Very High	High	High	Moderate	Moderate
Stand-still Performance	Very Good	Good	Good	Moderate	Moderate
Load Capacity	Low to Moderate	Moderate to High	Low to Moderate	Moderate	Moderate to High
Simplicity	Simple	Moderate	Simple	Simple	Moderate
Volume	Small	Moderate	Small	Small to Medium	Small to Medium

Table D.3: Type of actuators

D.1.3. General Sensors

Table D.4: Comparison of Different Types of Sensors

Sensor Type	Chromatic Confocal	Capacitive	Eddy Current	Linear Encoders	Laser Interferometry
Measuring Range	Medium to High	Low to High	Low to High	Low to High	Low to High
Sensitivity to External Conditions	Low	Moderate to High	Low to Moderate	Low to High	Low to Moderate
Ease of Use	Moderate	Moderate	Low to Moderate	Moderate to High	Moderate
Resolution	High	Moderate to High	Moderate	High	Very High
Volume	Medium	Small to Medium	Small to Medium	Medium	Medium
Costs	High	Low to High	Moderate to High	Low to High	High

Table D.5: Type of sensors

D.1.4. Morphological Overview

functions								
Flexural Guiding	Parallelogram 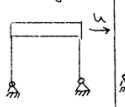	Roberts 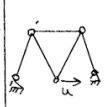	X-bob 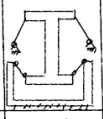	Peaucellier 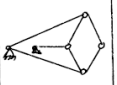	13-Hinge 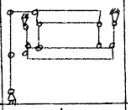	SArrus 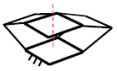	sx folded leaf springs 	orthoplanar spring 
Actuating	Piezo-electric	Electro-Static	Electro-magnetic	Electro-thermal	Electro-strictive	Pneumatic	Hydraulic	
Transmission (if needed)	Lever 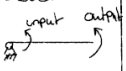	double sided Lever 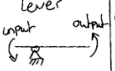	Triangle 					
control	Voltage Buffer	Driver	Current source					
Sensing	chromatic confocal	Capacitive	Eddy Current	Linear Encoders	Laser Interferometry			

D.2. Concept Validation

Each concept is compared to its kinematics, stiffness, and volume. These performance criteria are defined and optimized via fmincon in MATLAB. The kinematics, stiffness, and optimization method are generally defined.

D.2.1. Kinematics

The motion of all points can be mathematically defined. This is done by general definition of two circles that intersect:

$$I_{x_{12}} = \frac{x_1 + x_2}{2} + \frac{(x_1 - x_2)(r_1^2 - r_2^2)}{2d^2} \pm \frac{y_2 + y_1}{2d^2}\sqrt{((r_1^2 + r_2^2)^2 - d^2)(d^2 - (r_1 - r_2)^2)} \tag{D.1}$$

$$I_{y_{12}} = \frac{y_1 + y_2}{2} + \frac{(y_1 - y_2)(r_1^2 - r_2^2)}{2d^2} \pm \frac{x_2 + x_1}{2d^2}\sqrt{((r_1^2 + r_2^2)^2 - d^2)(d^2 - (r_1 - r_2)^2)} \tag{D.2}$$

With d, as the distance between the two circles:

$$d = \sqrt{(x_2 - x_1)^2 + (y_2 - y_1)^2} \tag{D.3}$$

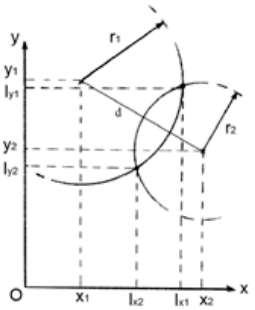

Figure D.1: Enter Caption

D.2.2. Stiffness Code

```
% Define geometric properties
alpha = 5; % Angle of beam to horizontal axis in deg
gamma = 27; % Angle of support beam to main beam in deg
L = 0.075; % Length of main beam in m
Ls = 0.0421; % Length of support beam in m
t = 0.0006; % Thickness of beam in m
d = 0.08; % Width of beam in m

% Cross-sectional properties
A = d * t; % Cross-sectional area in m^2
Iz = (1/12) * d * t^3; % Second moment of area (moment of inertia) in m^4
J = (1/12) * d * t^3; % Torsional constant in m^4
Iy = (1/12) * t * d^3; % Second moment of area about y-axis in m^4

% Material properties
E = 71.7e9; % Young's modulus in Pa
G = 26.4e9; % Shear modulus in Pa

% Define the coordinates of the nodes

 nodes = [0, 0, 0;    % Node 1
          L*cosd(alpha), L*sind(alpha), 0;
          Ls * cosd(alpha + gamma), Ls * sind(alpha + gamma), 0];

% Define the connectivity matrix for the truss structure
connectivity = [1 2
                1 3
                3 2];

% Calculate the lengths of each beam
num_beams = size(connectivity, 1);
lengths = zeros(num_beams, 1);

for i = 1:num_beams
    node_i = connectivity(i, 1);
    node_j = connectivity(i, 2);
    lengths(i) = norm(nodes(node_j, :) - nodes(node_i, :));
end

% Initialize the global stiffness matrix
num_nodes = size(nodes, 1);
num_dof_per_node = 6;
K_global = zeros(num_nodes * num_dof_per_node, num_nodes *
   num_dof_per_node);

% Loop through each beam to assemble its stiffness contribution
for i = 1:num_beams
    node_i = connectivity(i, 1);
    node_j = connectivity(i, 2);

    % Calculate the direction cosine matrix
    x = nodes(node_j, :) - nodes(node_i, :);
    theta = atan2d(x(2),x(1)); % atan2d ensures correct quadrant

    % Transformation matrix
```

```
    T = transformation_matrix(theta);

    % Element stiffness matrix in local coordinates
    ke_local = element_stiffness_matrix(E, G, A, Iz, Iy, J, lengths(i));

    % Rotate element stiffness matrix to global coordinates
    ke_global = T' * ke_local * T;

    % Define indices for the degrees of freedom (DOF) for each node
    start_i = 6 * (node_i - 1) + 1;
    end_i = 6 * node_i;
    start_j = 6 * (node_j - 1) + 1;
    end_j = 6 * node_j;

    % Update the global stiffness matrix
    K_global(start_i:end_i, start_i:end_i) = K_global(start_i:end_i,
        start_i:end_i) + ke_global(1:6, 1:6);
    K_global(start_i:end_i, start_j:end_j) = K_global(start_i:end_i,
        start_j:end_j) + ke_global(1:6, 7:12);
    K_global(start_j:end_j, start_i:end_i) = K_global(start_j:end_j,
        start_i:end_i) + ke_global(7:12, 1:6);
    K_global(start_j:end_j, start_j:end_j) = K_global(start_j:end_j,
        start_j:end_j) + ke_global(7:12, 7:12);
end
%
% Fix the degrees of freedom at node 3


% Remove the rows and columns of K_global corresponding to
    fixed_dof_node_3
K_reduced = K_global;
K_reduced(13:18,:) = [];
K_reduced(:,13:18) = [];

% Select stiffness corresponding to the degree of freedom at node 1
Kcc = K_reduced(1:12, 1:12);
Kcc(3:5,:)=[];
Kcc(:,3:5)=[];
Kcc(6:8,:)=[];
Kcc(:,6:8)=[];

%
% Applied force at node 1 (vertical force)
force_node_1 = [0; 1; 0; 0; 0; 0;];

%Calculate the displacement at node 1 (vertical displacement)
displacement_node_1 = Kcc \ force_node_1;

% Calculate the vertical stiffness at node 1
vertical_stiffness = force_node_1(2) / displacement_node_1(2);

disp('Vertical Stiffness at Node 1:');
disp(vertical_stiffness);

% Function to calculate the transformation matrix
function T = transformation_matrix(theta)
```

```
    T1 = [cosd(theta), -sind(theta), 0; sind(theta), cosd(theta), 0; 0, 0,
        1];
    T = blkdiag(T1, T1, T1, T1); % 4x4 block diagonal matrix
end

% Function to calculate the element stiffness matrix
function ke = element_stiffness_matrix(E, G, A, Iz, Iy, J, length)

ke = [A*E/length 0 0 0 0 0 -A*E/length 0 0 0 0 0;
                0 12*E*Iz/length^3 0 0 0 6*E*Iz/length^2 0 -12*E*Iz/length
                    ^3 0 0 0 6*E*Iz/length^2;
                0 0 12*E*Iy/length^3 0 -6*E*Iy/length^2 0 0 0 -12*E*Iy/
                    length^3 0 -6*E*Iy/length^2 0;
                0 0 0 G*J/length 0 0 0 0 0 -G*J/length 0 0;
                0 0 -6*E*Iy/length^2 0 4*E*Iy/length 0 0 0 6*E*Iy/length^2
                     0 2*E*Iy/length^2 0;
                0 6*E*Iz/length^2 0 0 0 4*E*Iz/length 0 -6*E*Iz/length^2 0
                     0 0 2*E*Iz/length;
                -A*E/length 0 0 0 0 0 A*E/length 0 0 0 0 0;
                0 -12*E*Iz/length^3 0 0 0 -6*E*Iz/length^2 0 12*E*Iz/
                    length^3 0 0 0 -6*E*Iz/length^2;
                0 0 -12*E*Iy/length^3 0 6*E*Iy/length^2 0 0 0 12*E*Iy/
                    length^3 0 6*E*Iy/length^2 0;
                0 0 0 -G*J/length 0 0 0 0 0 G*J/length 0 0;
                0 0 -6*E*Iy/length^2 0 2*E*Iy/length 0 0 0 6*E*Iy/length^2
                     0 4*E*Iy/length^2 0;
                0 6*E*Iz/length^2 0 0 0 2*E*Iz/length 0 -6*E*Iz/length^2 0
                     0 0 4*E*Iz/length;];
end
```

D.2.3. Optimization

The optimization problem can be formulated. The goal is to minimize the drive stiffness. This should be obtained while maintaining volume, error, stress, and manufacturability constraints. Most algorithms benefit from a minimization problem therefore it is rewritten into a negative null form:

Minimize

$$\frac{1}{C_x}$$

Subject to

$$e - 5 \times 10^{-9} \leq 0$$
$$\sigma_y - 150 \times 10^{6} \leq 0$$
$$Z_{vol} - 35 \times 10^{-3} \leq 0$$

and

$$\underline{\mathbf{x}} \leq \mathbf{x} \leq \bar{\mathbf{x}}$$

D.3. Concept 1: 13-Hinge

The 13-Hinge mechanism, initially introduced by Jones in 1956 (Jones and Young, 1956), comprises two four-bar linkage parallelograms arranged in series. These parallelograms, interconnected to a lever, traditionally induce synchronized movement, resulting in each parallelogram covering half of the total stroke relative to the other. The lever is linked to the parallelograms through two rods with a traditional ratio of ½ to each other. The system is mitigating parasitic movements through the compensation of the in-series connected parallelograms.

Noteworthy characteristics of this mechanism include its notable rectilinearity, elevated stiffness, and facile manufacturability attributable to its planar geometry.

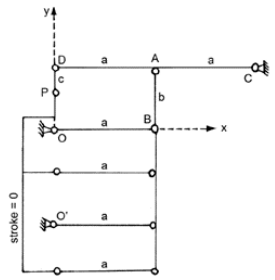

Figure D.2: Geometrical representation 13-Hinge

D.3.1. Kinematics

The horizontal error can be calculated, ϵ_{rect}.

$$\epsilon_{rect} = h_2 - h_1 = \sqrt{a^2 - (\frac{s}{2} - \delta)^2} - \sqrt{a^2 - (\frac{s}{2} + \delta)^2} \tag{D.4}$$

, with $\delta^2 \approx 0$. Resulting in:

$$\epsilon_{rect} = \sqrt{a^2 - (\frac{s^2}{4} - s\delta)^2} - \sqrt{a^2 - (\frac{s^2}{4} + s\delta)^2} \tag{D.5}$$

, with $\delta = B_y - \frac{s}{2}$.

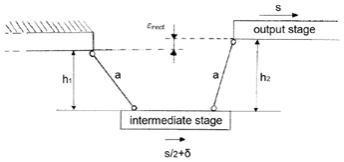

Figure D.3: Error representation intermediate part and end effector

The functions above can confirm the traditional ratio $R = \frac{c}{b} = \frac{1}{2}$. The plot below shows a minimal error at $R = \frac{1}{2}$

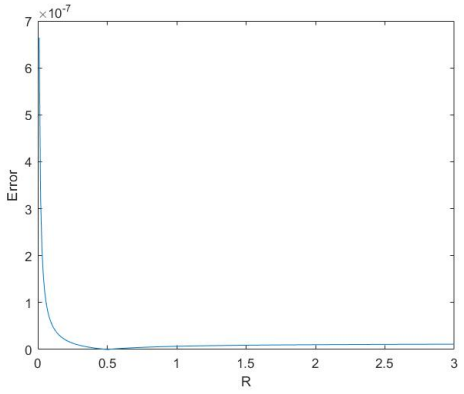

Figure D.4: Error vs Ratio plot, minimum at R=0.5

D.3.2. Optimization Results

The optimization results are $a = 0.0515$ m, $b = 0.01$ m. Furthermore, the thickness is $t = 0.3$ mm,the width of the slender beams are $d = 0.1$ m, and the distance between the slender beams is $r = 0.0155$ m. Resulting in a volume of 103x100x33 [mm].

Implementing the defined coordinates of previous section into the earlier defined MATLAB script. The drive and support stiffness are $C_z = 9985$ N/m and $C_x = 1.2E8$ N/m.

D.4. Concept 2: Peaucellier

The Peaucellier-Lipkin straight-line mechanism is a mechanical linkage designed to achieve near-perfect straight-line motion. It is a planar, six-bar linkage that was independently developed by Charles-Nicolas Peaucellier and Yom Tov Lipkin in the 19th century. The mechanism is particularly noteworthy for its elegant simplicity in converting circular motion into precise straight-line motion.

The working principle of the Peaucellier-Lipkin mechanism is based on a mathematical concept known as inversion. It exploits the fact that when a point on a circle undergoes circular motion, its inverse point on another circle will follow a straight-line path. In the Peaucellier-Lipkin linkage, a circular motion is transformed into linear motion by utilizing a carefully arranged series of six connected bars with specific geometric properties. The key element is a diamond-shaped configuration formed by four bars, with one bar acting as a coupler. This coupler traces an approximate straight-line path as the mechanism undergoes circular motion. When the linkage is appropriately designed and constrained, the result is a mechanism that can accurately generate linear motion, making it an ingenious solution for achieving straight-line.

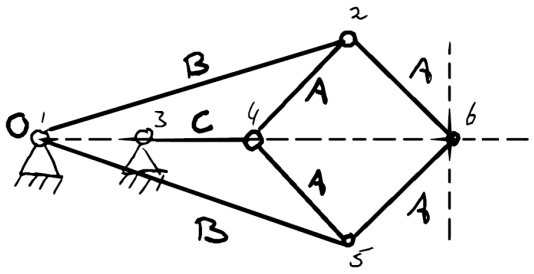

Figure D.5: Geometric representation Peaucellier

D.4.1. Kinematics

The X position of node 6 can be calculated as, ϵ_{rect}:

$$\epsilon_{rect} = \frac{B^2 - A^2}{2C} \tag{D.6}$$

D.4.2. Optimization Results

The optimization results are $A = 0.06$ m, $B = 0.0911$ m, and $C = 0.0158$ m. Furthermore, the thickness is $t = 0.4$ mm and the width of the slender beams are $d = 0.21$ m. Resulting in a volume of 148x210x26 [mm].

Implementing the defined coordinates of previous section into the earlier defined MATLAB script. The drive and support stiffness are $C_z = 5000$ N/m and $C_x = 2.6E6$ N/m. Concluding that there was no solution found for the defined contraints. The support stiffness was relaxed.

D.5. Concept 3: Sarrus

The Sarrus linkage is dated from 1853 when it was invented by Pierre Frederic Sarrus (Waldron et al., 2016). The linkage, comprising four equal length links organized into two perpendicular groups,

is characterized by its utilization of two parallel horizontal plates arranged vertically, one above the other. Each group features pairs of hinged bars or plates connecting the horizontal plates, facilitating vertical motion of the upper plate towards and away from the lower one. The hinges enforce constraint, ensuring the connected bars or plates remain in the same plane and maintain axial translation.

Notably, the Sarrus linkage falls within the three-dimensional category. An advantageous feature is its capacity to elevate the structure connecting the upper links, thereby enabling a diverse range of movements. Mobility analysis indicates a Degree of Freedom of 0 for the 2-sided Sarrus linkage; however, due to over constraint, the upper platform exhibits vertical mobility.

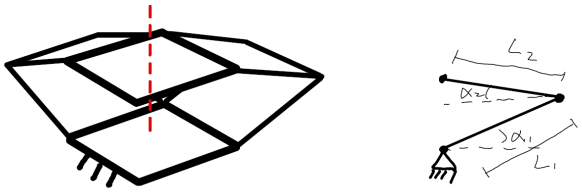

Figure D.6: Geometrical representation Sarrus

D.5.1. Kinematics

When beam 1 has the same length and orientation as beam 2, there is no mathematical error. However, there are asymmetric configurations possible. The horizontal motion of the beams should cancel each other out, so related to finding the balance in stiffness.

D.5.2. Optimization Results

The optimization results are $L1 = 0.0959$ m, $L2 = 0.1$ m, $\alpha_1 = \alpha_2 = 0.2637$rad . Furthermore, the thickness is $t = 0.4$ mm,the width of the slender beams are $d = 0.0903$ m. Resulting in a volume of 190.3x190.3x25 [mm].

Implementing the defined coordinates of previous section into the earlier defined MATLAB script. The drive and support stiffness are $C_z = 555$ N/m and $C_x = 1.3E7$ N/m.

D.6. Selection Matrix

The design criteria and their weighting factors (-) are:

- Theoretical straightness: The mathematical straightness of the desired motion. This is most important for the application. (5x)
- Conservative orientation: This defines if the mechanism enables linear motion of a point or a body. Important because a body has to be moved, nevertheless a moving point can be transferred to a body (using two or three mechanisms for instance). (4x)
- Angular stroke: Angular stroke is the maximum angle the beams make to create the motion. This give insight in how suitable the mechanism is to transform to a compliant mechanisms. (2x)
- Overconstraints: These are determined by Grueblers' equation. Typically overconstraints are unwanted if the parastic motions have to be minimized. However, if, for instance, the stiffness has to be improved. Overconstraints can be beneficial. (3x)
- Easy of modelling: An optimal design is desired. Therefore, the modelling is preferred to be easy to reduce computation time and the number of iterations can be improved. (2x)
- Geometry: In terms of manufacturability, the design is more easy to manufacture when the design is planar instead of spatial. (2x)
- Volume in drive direction: The volume is limited in the drive direction. Increasing the volume is dependent on the client. (2x)
- Cost: The costs should remain low as it is a proof of concept. From a commercial perspective it is important to minimize the costs as well. (3x)

- Tolerance sensitivity: This is determined via ARTAS SAM 8.4. The parameter with most influence is found, and the effect on the simulated straightness is determined. (3x)
- Complexity: The number of thin joints is considered as a way of measuring the complexity of the design. It is preferred to keep the design as simple as possible, while this improves the confidence in the later design to reach nanometer accuracy. (4x)
- Support stiffness: A certain amount of support stiffness must be achieved. This is determined by that the mechanism can follow the external vibrations so that there is no error made there. (4x)
- Drive stiffness: A maximum is set for the drive stiffness. This to reduce the actuator force needed for the motion. A smaller actuation force results in less internal stresses and deformations which can lead to errors. (2x)

Selection Criteria	Weighting Factor			Concept 1			Concept 1	Concept 2	Concept 3
		--	-	0	+	++			
Kinematics									
Theoretical Straightness	5	>5E-9	>2E-13	2E-13 [m]	0		0	+	+
Conservative orientation	4	Point		Body			0	- -	0
Angular Stroke	2	>8deg	>1.5deg	1.5deg	<1.5deg		0	- -	+
Overconstraints	3	>5	>2	0			0	0	-
ease of modelling	2			Non-Sym	Symmetry		0	0	+
Design									
Geometry	2		Spatial	Planar			0	0	-
Volume in Drive Direction	2		>33 [mm]	33 [mm]	<33 [mm]		0	+	+
Cost	3						0	-	+
Tolerance Sensitivity	3		>27 [nm] or unknown	27 [nm]	<20nm	<15nm	0	+	-
Complexity	4	>8 thin joints	>6 thin joints	6 thin joints	<6 thin joints	<4 thin joints	0	-	++
Performance									
Support Stiffness	4	<1.2E7	<1.2E8	1.2E8 [N/m]	>1.2E8		0	- -	-
Mechanism Drive Stiffness	2	>15000	>9985	9985 [N/m]	<9985	<5000	0	+	++
						Total	0	-15	14

E

HEEDS MDO

To find the optimal design of the torsion reinforced Sarrus mechanism, a new software package is introduced within VDL ETG T&D Eindhoven. The software, named HEEDS MDO, is a multidisciplinary design exploration and optimization software package of Siemens.

HEEDS MDO can help to gain an insight in the design space, and could find an optimal design according to multiple design criteria and constraints. HEEDS MDO is combined with other packages, for instance of Siemens: NX and NASTRAN. NX is used to define a conceptual sketch. Thereafter, a mesh and simulation is generated with NASTRAN. These three files are used by HEEDS MDO to optimize and explore the design and design space. The benefits of HEEDS MDO are that it is not needed to be an expert in optimization theory, and when experienced, the design iteration process is automated and accelerated. The optimal design is the best possible design using the specific parameters, and this is supported by a lot of user-friendly post-processing.

To generate the optimal design for the Sarrus mechanism, several steps must be taken. First, a conceptual sketch with the basic shapes must be drawn in NX. Second, a converged and robust mesh must be made within NASTRAN. Thereafter, the optimization problem must be defined and implemented in HEEDS MDO. To run the study, the suitable optimization algorithm must be chosen. Furthermore, a Design of Experiments can be done to gain an insight into the design space of the parameters. A parameter optimization can be made once the sketch, mesh, optimization problem, and algorithm are made and chosen. Lastly, a lot of post processing can be done to visualize the optimization process and design space.

E.1. Parameter Sketch

HEEDS needs a sketch that is based on the design parameters. So a parametric sketch has to be created, where the dimensions and/or constraints are defined as variables. The variables are then linked to HEEDS, and new designs can be generated within the variable boundaries.

E.2. Meshing

Meshing is the stage of the finite element modelling process in which you divide a continuous structure (in this case the Sarrus mechanism) into a finite number of regions. These regions are known as elements and are connected together by nodes (“Siemens Simcenter 3D Pre/Post”, 2022). Each element:

- Is a mathematical representation of a discrete portion of the model’s physical structure.
- Has an assumed displacement interpolation function.

The accuracy of the mesh is important while the results depends partly on the quality of the mesh. In this case, the results are in the order of nanometers making the mesh quality even more important. The combination with HEEDS MDO asks for a converged, controlled, and robust mesh while for each

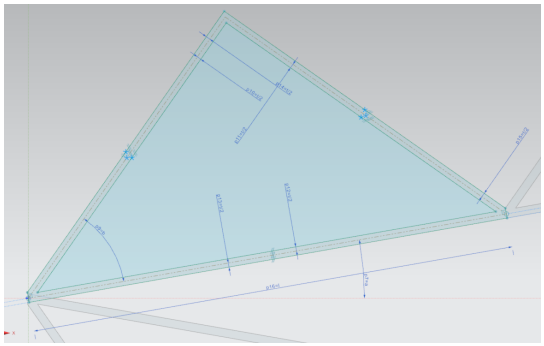

(a) Sketch

1	Default Gro...					
2				mm	Length	Number
3	a	10	10	°	Angle	Number
4	b	45	45	°	Angle	Number
5	b2	45	45	°	Angle	Number
6	d	150	150	mm	Length	Number
7	g	20	20	°	Angle	Number
8	l	L1/n	17.5	mm	Length	Number
9	L1	70	70	mm	Length	Number
10	l2	L_2/n2	17.5	mm	Length	Number
11	L_2	70	70	mm	Length	Number
12	n	4	4		Unitless	Number
13	n2	4	4		Unitless	Number

(b) Parameter Table

Figure E.1: Parametric Sketch

design HEEDS MDO creates the mesh quality should be high.

For the Sarrus mechanism, three types of elements are used: 0D, 2D (shell), and 3D (solid) elements. All the connections between the elements are controlled by mesh controls to ensure a converged and robust high quality mesh.

A 0D mesh ensures a points-based element at specific nodes. This is needed to include a concentrated mass elements and can fungate as point of engagement. In this case, it is used as the point where the actuator force will act.

2D elements are commonly known as shell or plate elements. In this case, the 2D mesh is used to create a more easy to control surface compared to a 3D solid. If a 2D mesh is created on the surfaces first, the 3D mesh will use the existing 2D mesh as a starting point from which to create (“seed”) the 3D elements through the body.

An other application for a 2D mesh is to mesh the flexures as shell. The commonly used requirement to use shell elements is that the length characteristic must be way larger than another parameter: L»d, for instance. The benefit of using shell elements is the reduction of computation time relative to solid elements, while maintaining accuracy. This could be beneficial for HEEDS MDO while the computation time will be way less, and still an insight is obtained of the design space. However, for optimization of the Sarrus mechanism the accuracy of 2D elements was insufficient while the filets where not included. The results partly depends on these fillets, that is why the flexures were meshed with 3D elements

Achieving mesh convergence is crucial for ensuring the accuracy, stability, and reliability of computational simulations. It is important to control this convergence by mesh controls. HEEDS will create a mesh on its own based on these controls. Therefore, strict controls must be applied to be sure that HEEDS will always generate a mesh that is converged.

E.3. Optimization Problem

The optimization problem can be formulated. The goal is to maximize the difference between the first eigenmode and second parasitic eigenmode. This should be obtained while maintaining volume, error, stress, and manufacturability constraints. Most algorithms benefit from a minimization problem therefore it is rewritten into a negative null form:

Minimize

$$\frac{f_0}{f_1}$$

Subject to

$$f_0 - 20 \leq 0$$
$$e - 5 \times 10^{-9} \leq 0$$
$$\sigma_y - 150 \times 10^6 \leq 0$$
$$Z_{vol} - 45 \times 10^{-3} \leq 0$$

and

$$\underline{\mathbf{x}} \leq \mathbf{x} \leq \bar{\mathbf{x}}$$

E.4. Algorithm

HEEDS MDO supports several known optimization algorithms: genetic algorithm, nondominated sorting genetic algorithm, quadratic programming, simulated annealing, response surface, multi start local search, particle swarm optimization, and Nelder-Mead simplex. In addition, HEEDS contains a unique search strategy called SHERPA, which stands for Simultaneous Hybrid Exploration that is Robust, Progressive, and Adaptive.

SHERPA employs a multi-faceted approach during a single search, utilizing multiple search methods. This strategy leverages the strengths of each method while dynamically diminishing the involvement of ineffective methods throughout the search process (Chase et al., 2010). A combination of global and local search methods is integrated, each equipped with tuning parameters that undergo automatic adjustments based on evolving knowledge of the design space. The adaptive nature of SHERPA enables it to learn efficiently about the design space, determining when and to what extent each method is utilized. While it does not claim that this approach is better or guarantees of always finding a global optimal solution, this approach has demonstrated notable effectiveness and efficiency across various practical engineering design problems. Key advantages include the alleviation of the following concerns:

- Users are spared the need to invest time and effort in comprehending their design space prior to selecting an optimization algorithm
- Limited expertise in optimization algorithms and applications is required from users
- Users can realistically define problems based on actual engineering or business costs and benefits without being constrained by the capabilities of a specific search method, allowing for broader problem definitions encompassing a larger number of variables.

F

Measurement Setup

F.1. Voice Coil Actuator

A standard voice coil actuator is used, Akribis AVM40-HF-6.5. Voice coil actuators operate based on the principle of Lorentz force. When an electrical current passes through a coil of wire placed within a magnetic field, a force is exerted on the coil, causing it to move linearly. This permanent-magnet direct drive actuator operates without backlash and cogging.

- Direct linear motion
- High resolution
- Zero cogging
- Zero backlash
- Rapid response
- No wear and tear
- Smooth motion at low speeds

F.1.1. Drive system

Attributes

- Waveform generator: VDL EDEV
- Power supply: VDL EDEV Lab
- Operational Amplifier (OPAMP): Texas Instruments LM3886TF
- Voice Coil Actuator: AVM40-HF-6.5 (see spec. sheet)

Problem Statement

Voice coil has to move +-2.5mm. A force of 6[N] is needed as gravity compensation and 2[N] for the 2.5[mm] stroke.

Solution Description

Waveform generator is saturated at +-0.1A. Voice coil requires a current of 0.29+0.095[A] to achieve 6+-2[N]. Therefore, a voltage follower is needed to provide this current. A realisation of such a voltage follower is shown below by using an OPAMP.

The main power supply consists of a power supply and a waveform generator. If possible, only a waveform generator can be used as the offset voltage can be provided by this, to achieve 10 N.

The actuator schematically exists of a series connection of resistance and inductance. Inductance is negligible, since the frequency is 0.1 Hz, very low: $Z_L = j\omega L \approx 0$.

Calculations

$$F = 6 \pm 2[N] \tag{F.1}$$

$$F = 20.7 * I \tag{F.2}$$

$$I = 0.29 \pm 0.095[A] \tag{F.3}$$

$$U = IR_L \tag{F.4}$$

$$U = 3.19 \pm 1.045[V] \tag{F.5}$$

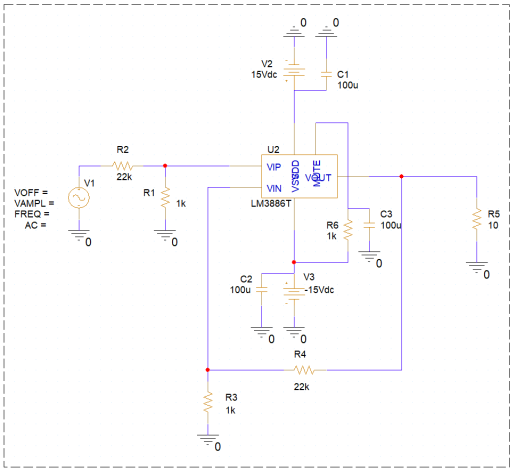

Figure F.1: Electronic circuit for OPAMP with gain 1

F.2. Chromatic Confocal Sensors

The chromatic confocal sensor is a non-contact measurement instrument known for its high precision. Its capability extends to measuring parameters such as displacement, thickness, distance, flatness, and roughness by harnessing chromatic lights of varying wavelengths. Operating on the principle of chromatic aberration within optical systems, these sensors employ polychromatic light directed onto a lens, thereby creating a spectrum of wavelengths. The resulting spectrum enclose diverse focus points where the dispersed light converges. The light incident at the intersection point of the optical axis and the object's surface can traverse the spectrometer through mechanisms like a beam splitter and filtering pinhole. Notably, only the focused light contributes to the spectrometer, and by scrutinizing the detected wavelength, the sensor accurately determines the distance from itself to the object.

Advantages:

- High speed suitability
- High resolution
- Stable on all surfaces
- More stable than laser triangulation or eddy current sensors
- Sensing under angle is possible

Disadvantages:

- Relative small measuring range
- Beam path must be relatively clean
- Perform poorly with lots of change in surface conditions; cleanliness, roughness, etc..

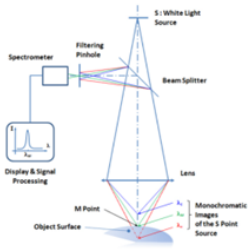

Figure F.2: Chromatic confocal principle

F.3. Measuring Frame

All subsystems are integrated into one measurement setup. The setup consists of a aluminum frame and base plate, 3D- printed sensor and actuator interfaces, the actuator, the sensors, and the mechanism itself. The setup stands on rubber adjustable feet, on a vibration isolation table of TMC from 3 Hz with minimal amplification of resonance (8-12dB).

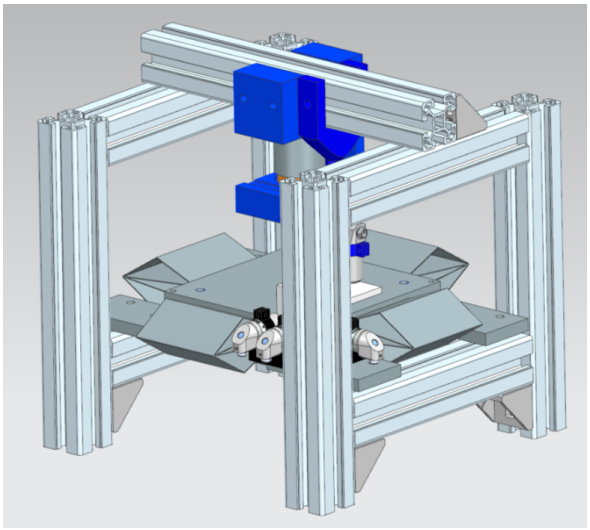

(a) CAD

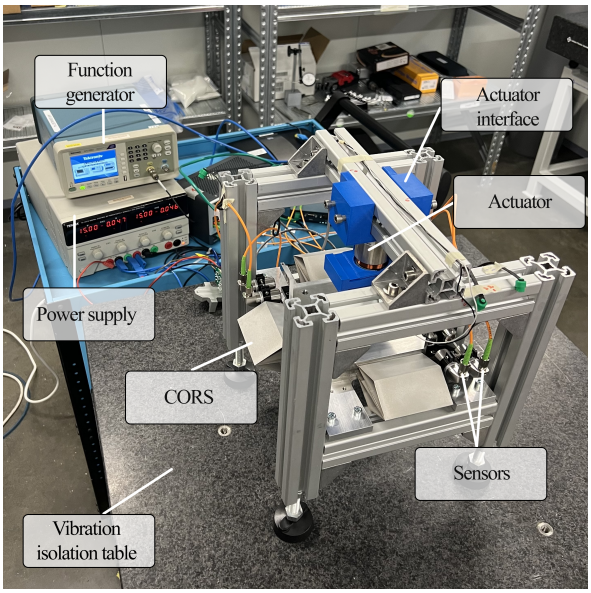

(b) Test setup

Figure F.3: Test setup

F.4. Drawings

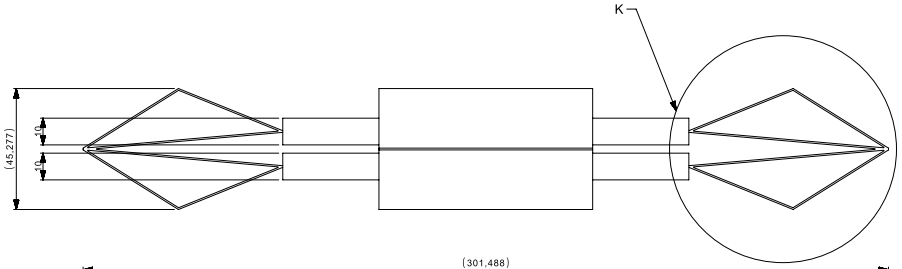

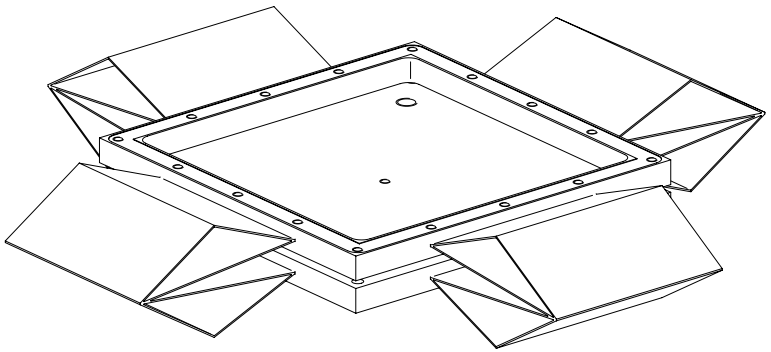

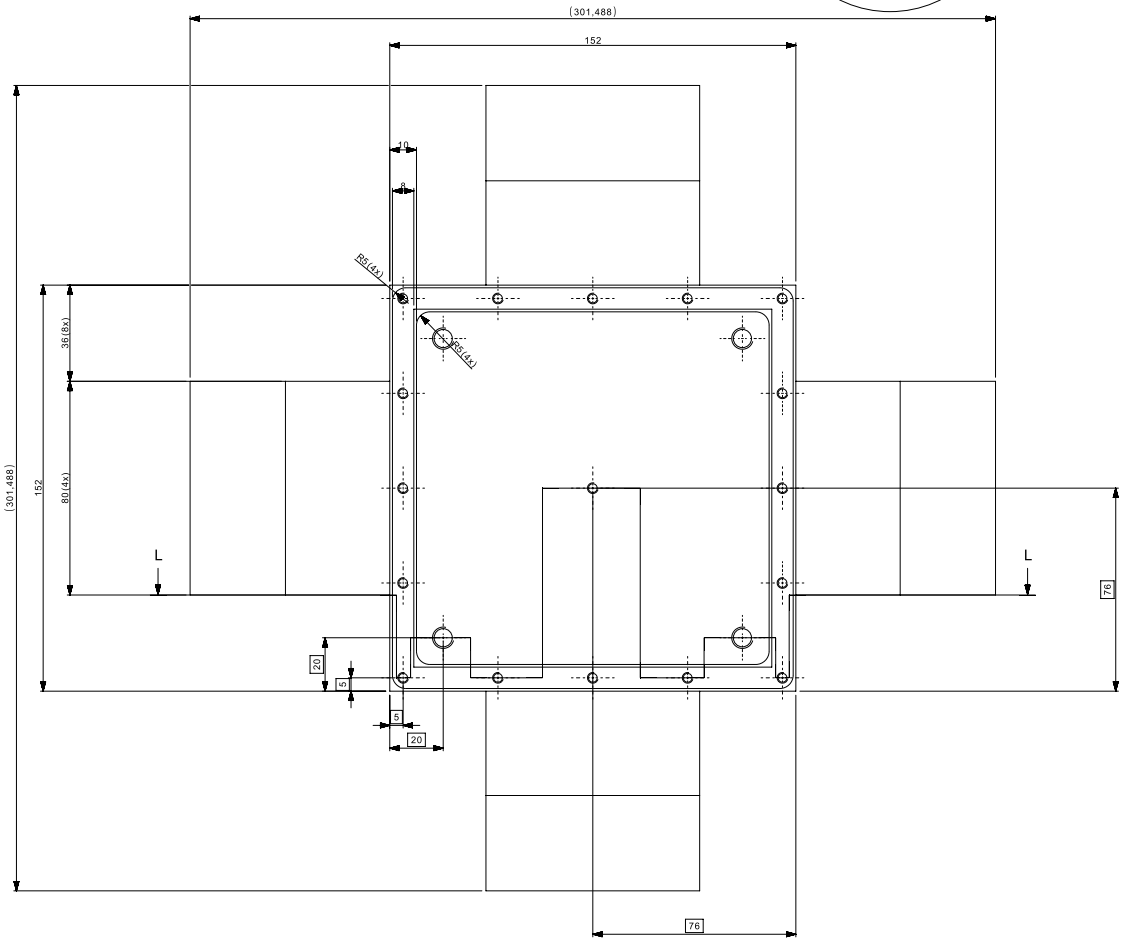

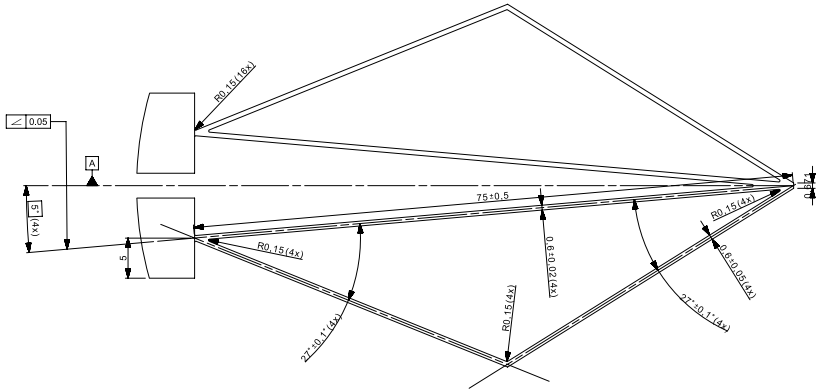

K
(3:1)

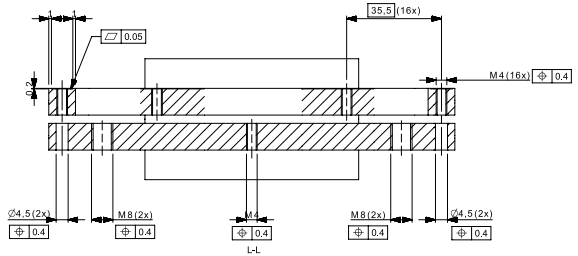

MATERIAL: EN-AW 5083-O; cast and homogenized, standard grade [VE4_FormMaterial]			SCALE: 1:1	PROJ.
TREATMENT: -			GENERAL ROUGHNESS: Ra 4 ISO 1302	UNIT: mm
ITEM NAME: Compliant Ultra-Rectilinear Stage		ITEM ID: -		ITEM REV.: A
STATUS	STATUS DATE	OWNER: Joran van Velden	GROUP NO:	SIZE: A1 PAGE: 1/1
VDL Enabling Technologies Group				

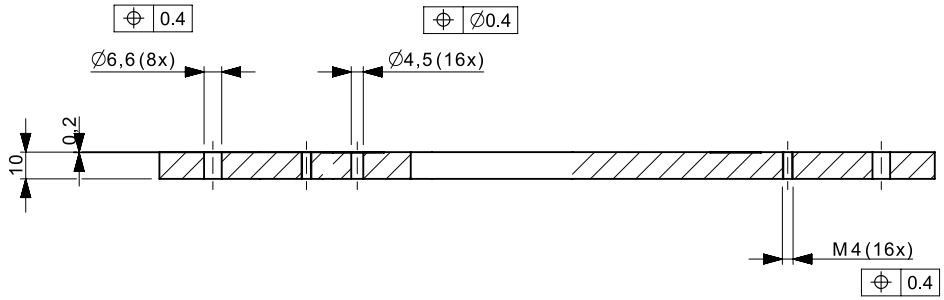

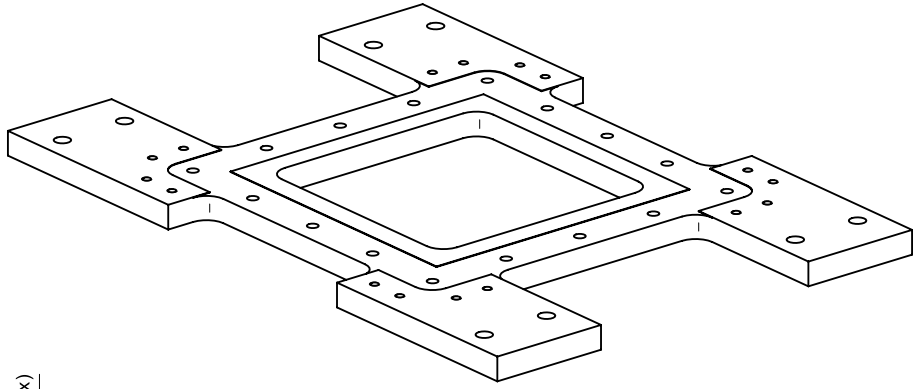

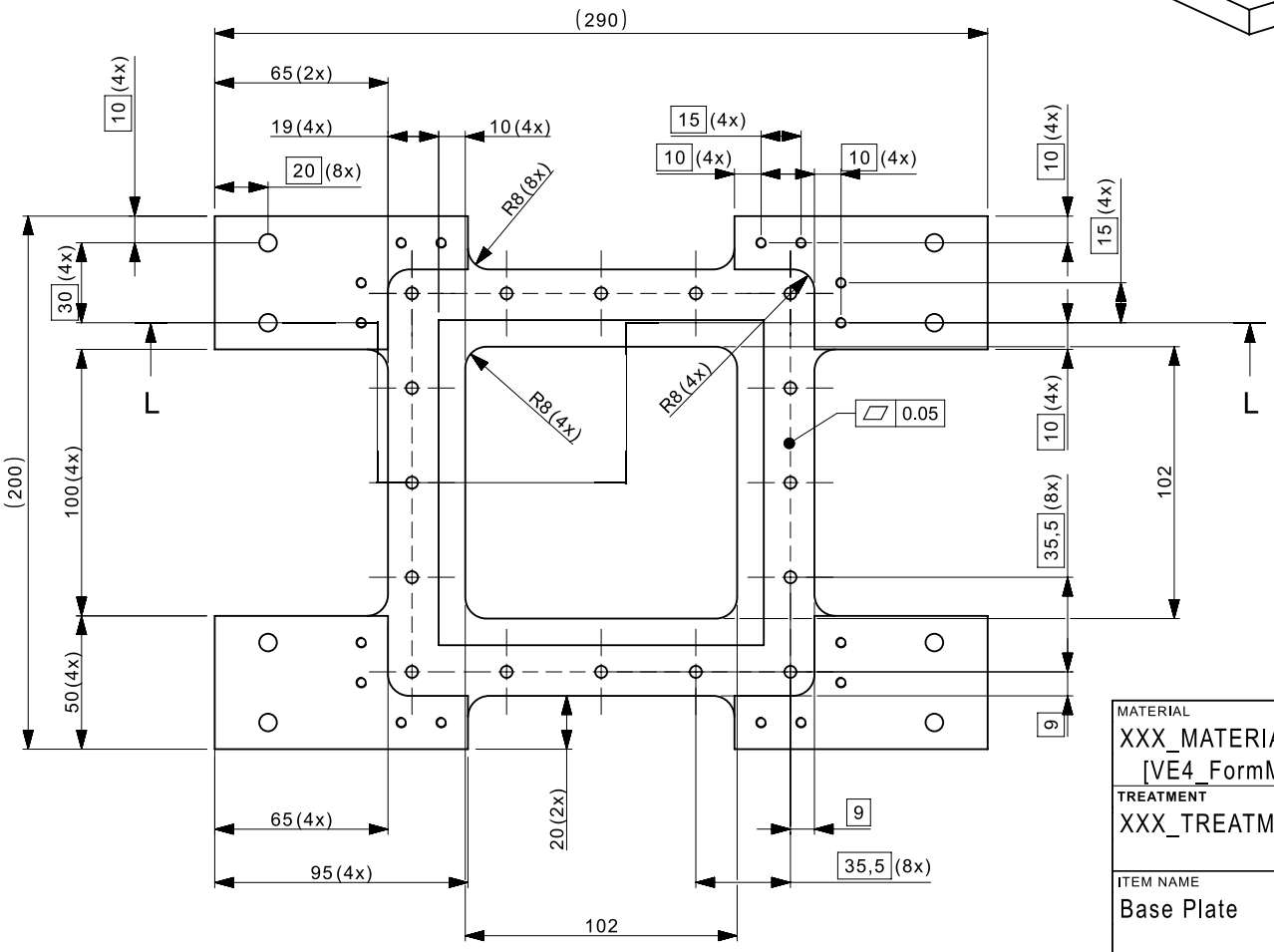

MATERIAL XXX_MATERIAL [VE4_FormMaterial]			SCALE 1:2	PROJ.
TREATMENT XXX_TREATMENT			GENERAL ROUGHNESS Ra 3.2 ISO 1302	UNIT mm
ITEM NAME Base Plate		ITEM ID ################		ITEM REV. A
STATUS	STATUS DATE	OWNER	GROUP NO.	SIZE A3 PAGE 1/1
VDL Enabling Technologies Group				

G

Manufacturability

G.1. Wire Electric Discharge Machining

Electric Discharge Machining (EDM) is a manufacturing process used to shape and fabricate metal parts with a high degree of precision. EDM operates by utilizing electrical discharges (sparks) to remove material.

EDM works on the principle of erosion, where a controlled electrical discharge between two electrodes (the tool and the workpiece) removes material from the workpiece through a series of rapid and repetitive sparks. Deionized water is used to facilitate the spark erosion process and to flush away debris. When the wire and the workpiece are brought into close proximity, a high-voltage electrical potential is applied between them. This creates a series of electric discharges or sparks between the two electrodes. The intense heat generated by these electrical discharges melts tiny portions of the workpiece material, which are then flushed away by the deionized water. The repeated action of the sparks gradually erodes the workpiece material, shaping it according to the desired design programmed into the machine's control system.

G.2. First prototype

The first prototype consisted of two flexures. This one failed due to the manufacturing strategy and design complexity.

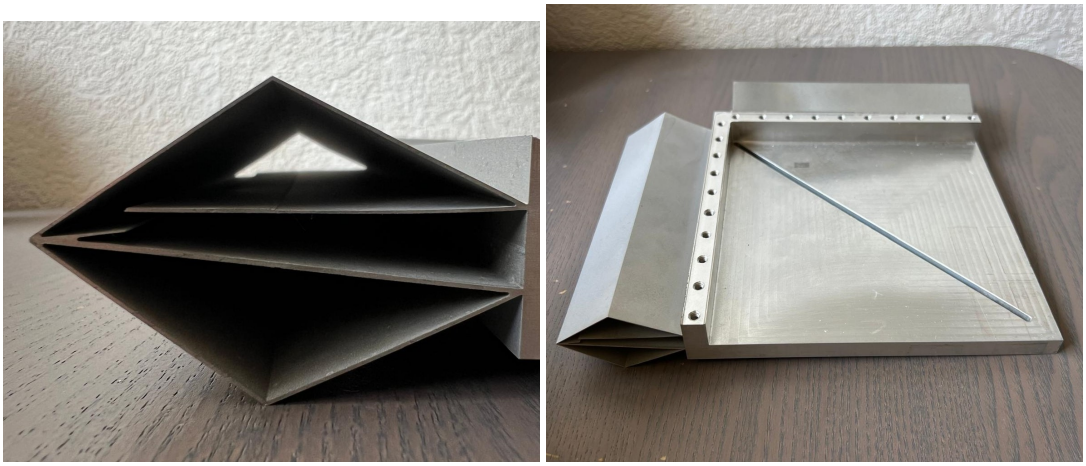

(a) Side view, with broken flexure

(b) Overview

Figure G.1: Pictures of 1st prototype

G.3. Second prototype

The second prototype consisted of four flexures. This to reduce the design complexity.

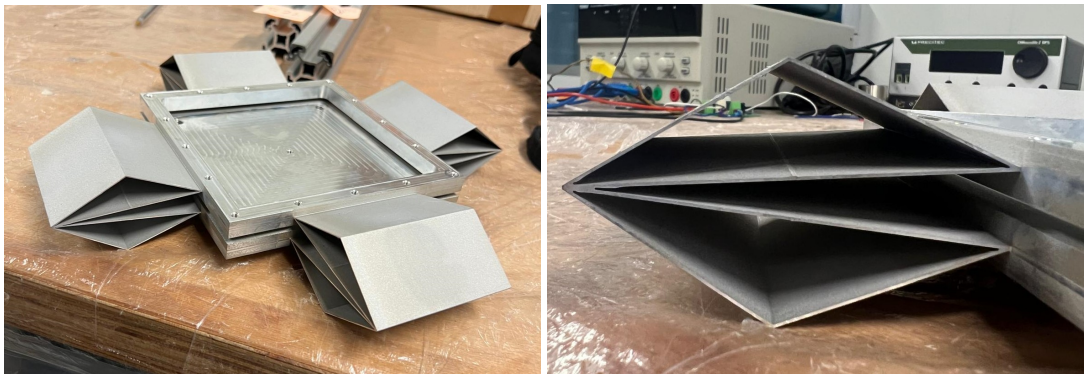

(a) Side view (b) Overview

Figure G.2: Pictures of used prototype

G.4. Lessons learned and questions

The lessons learned are:

- The sparks height must be minimized. The smaller the distance between the nozzles the smaller the wire vibrations are. Furthermore, a smaller distance results in better flushing of the debris.
- The eroding speed must be chosen properly. If the process goes to fast, the process loses its accuracy leading to defects. It is a trade-off between costs and accuracy.
- Larger fillets R>0.015 results in a faster and more precise process.

There are multiple questions that have arisen during manufacturing:

1. Was the aluminum work piece stress-free after milling?
2. What is the effect of the flexibility during the last spark erosions where the parts are separated from each other?
3. How to lower the surface roughness?
4. In the case that the flexure are misaligned, is it possible to correct the planes by milling so that the base plate and mask are again parallel to each other?
5. Does the milling influence the internal stresses of the workpiece?

All these questions need further development of the manufacturing process and experience.

H

Test Plan and additional experiments

H.1. Test Plan

H.1.1. Function Test Preconditions

Clean environment (similar to clean room ISO class 7) and a stable temperature (21 +/- 1 °C) External disturbances to the system should be minimized like vibrations, acoustic and EMI noise

H.1.2. Calibration

The sensors must be placed into their measuring range of 1.2 mm. This is done by hand, and tightening the screw when in and halfway the measurement range.

Thereafter, the actuator can be calibrated. The input voltage must be high enough to create a repeatable motion of at least 100 μm.

H.1.3. Functional Tests

Test ID	Test Title	Test Description	Prerequisites
1	Stand-still vibrations and drift	Measuring stand-still vibrations and drift over 180seconds. Repeat for all DoF	1) Fully assembled system mounted on an active isolation table; 2) Logging sensors in halfway measuring range
2	Modal Analysis	Measuring the eigenfrequencies by triggering the mask	1) Fully assembled system mounted on an active isolation table; 2) Logging sensors in halfway measuring range
3	Parasitic Motion Rx, Ry	Measuring the parasitic motions during a stroke of 100 μm	1) Fully assembled system mounted on an active isolation table; 2) Logging sensors in halfway measuring range; 3) Active Actuator with 0.1Hz, Offset of -1.1V and 400mV amplitude
4	Parasitic Motion X,Y, Rz	Measuring the parasitic motions during a stroke of 100 μm	1) Fully assembled system mounted on an active isolation table; 2) Logging sensors in halfway measuring range; 3) Active Actuator with 0.1Hz, Offset of -1.1V and 400mV amplitude
5	Functional stroke	Measure if the stroke of 2.5mm is possible	1) Fully assembled system mounted on an active isolation table; 2) Logging sensors in halfway measuring range; 3) Active Actuator with offset of 6.5V

H.2. Additional Experiments

H.2.1. Adding Mass

The effect of adding mass is investigated while there is a mirror placed on top of the mask. Therefore, a balancing mass was placed to compensate. The influence can be seen in the Table below.

Test ID	Mass	Mass Position	Ry
1	100g	(X;Y)=(76;0)	-184E-07 rad
2	300g	(X;Y)=(76;0)	-143E-07 rad

The difference is data is within the noise. Thus, it suggests adding mass has little to zero influence. However, additional research has to prove this.

H.2.2. Angled actuator force

The actuator is replaced multiple times. This to check the influence of a shear force onto the mechanism. An attempt has been made to create no X-translation. The effect can be seen in the Figure below.

As can be seen, the alignment of the actuator force has influence. Thus, it can be calibrated to create no translational error in X. Keep in mind, that it is possible that the mechanism is now facing parasitic motions in X, but due to misaligned mirrors these cancel each other out.

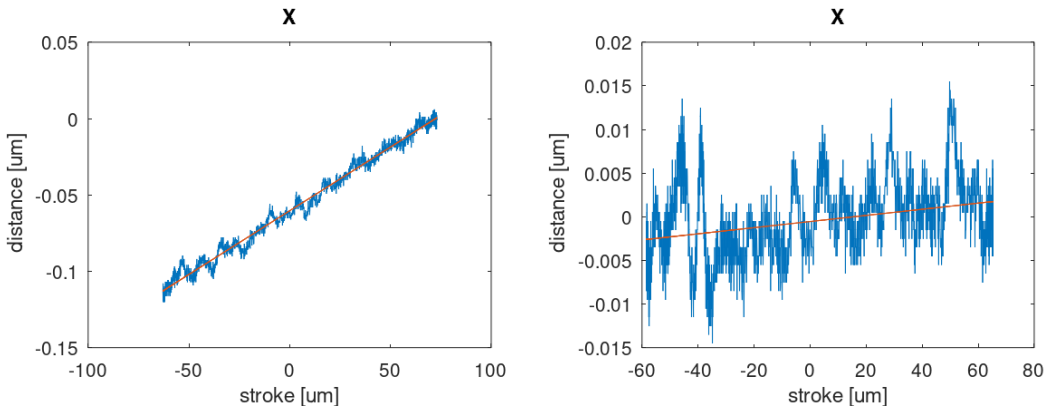

(a) No actuator correction

(b) Actuator correction

Figure H.1: X-translation without and with actuator correction

H.2.3. Assembling

Some tests were done to gain insight in the effect of assembling the system. Originally, the mechanism is screwed onto the base plate by 16 screws. Furthermore, the base plate has 8 screws connecting it to the measurement frame. The number of tightened screws is varied that there are three supporting points, there are four combinations possible. The results can be seen in the table below.

Test ID	Part	Assembled	Ry
1	Base Plate	Screwed on three rings	-159E-07 rad
2	Base Plate	Screwed on eight rings	-135E-07 rad
3	Sarrus guide	Screwed with thee screws	-173E-07 rad
4	Base Plate & Sarrus guide	Screwed with thee screws	-165E-07 rad

There is no clear relation between the assembling method and performance found.

H.2.4. Sample Rate

The effect of changing the sample rate can be seen in the level of noise and density of the measurement. There is measured at 400 Hz and 4000 Hz

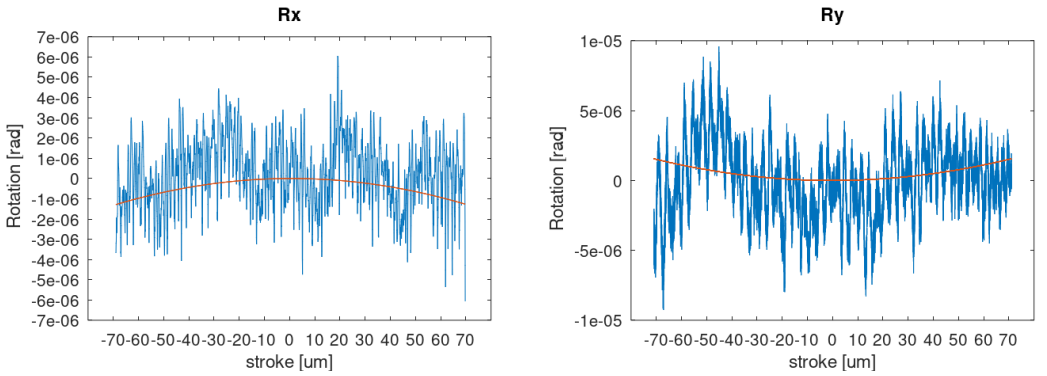

(a) Rx at 400 Hz

(b) Rx at 4000 Hz

Figure H.2: Measurements 400 Hz vs 4000 Hz

Error Calculations

Misalignment mirrors

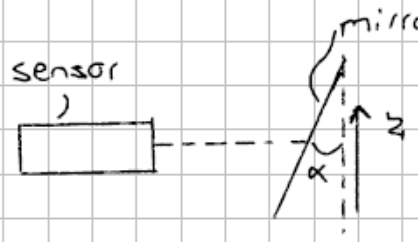

$z_1 = 140\ \mu m$

$\alpha = 1\ mrad$

$e = \sin\alpha \cdot z_1$

$e = 140\ nm$

Flatness mirrors

$$d = \text{flatness} \cdot \frac{\text{offset}}{\text{mirror radius}}$$

$$d = \frac{\lambda}{20} \cdot \frac{600\,\mu m}{600\,\mu m} = \frac{\lambda}{20}$$

(assuming flatness of mirror)

$$d = \frac{500\ nm}{20} = 25\ nm$$

Bibliography

Chase, N., Rademacher, M., Goodman, E., Averill, R., & Sidhu, R. (2010). A benchmark study of optimization search algorithms. *Red Cedar Technology, MI, USA*, 1–15.

Jones, R., & Young, I. (1956). Some parasitic deflexions in parallel spring movements. *Journal of Scientific Instruments*, *33*(1), 11.

Siemens Simcenter 3D Pre/Post. (2022).

Solak, H. H., & Ekinci, Y. (2005). Achromatic spatial frequency multiplication: A method for production of nanometer-scale periodic structures. *Journal of Vacuum Science & Technology B: Microelectronics and Nanometer Structures Processing, Measurement, and Phenomena*, *23*(6), 2705–2710.

Talbot, H. (1836). Lxxvi. facts relating to optical science. no. iv. *The London, Edinburgh, and Dublin Philosophical Magazine and Journal of Science*, *9*(56), 401–407. https://doi.org/10.1080/14786443608649032

Waldron, K. J., Kinzel, G. L., & Agrawal, S. K. (2016). *Kinematics, dynamics, and design of machinery*. John Wiley & Sons.